PRESSURE-TEMPERATURE-TIME-DEFORMATION HISTORY OF THE LAHUL VALLEY, NW INDIAN HIMALAYA

A Thesis submitted to the faculty of
San Francisco State University
In partial fulfillment of
the requirements for
the Degree

Master of Science

In

Geosciences

by

Andrew Robert Nieblas

San Francisco, California

May 2016

CERTIFICATION OF APPROVAL

I certify that I have read Pressure-Temperature-time-deformation history of the Lahul Valley, NW Indian Himalaya by Andrew Robert Nieblas, and that in my opinion this work meets the criteria for approving a thesis submitted in partial fulfillment of the requirement for the degree Master of Science in Geosciences at San Francisco State University.

Mary Leech, Ph.D.
Associate Professor of Geology

Jason Gurdak Ph.D.
Associate Professor of Geology

David P. Mungay for Karen Grove (Dept. Chair)
Karen Grove Ph.D.
Emeritus Professor of Geology

Pressure-Temperature-time-deformation history of the Lahul Valley, NW Indian Himalaya

Andrew Robert Nieblas
San Francisco, California
2016

The central Himachal crystalline of the NW Himalaya is a unique region characterized by broad shear along a decentralized section of the South Tibetan Detachment (STD). New $^{40}Ar/^{39}Ar$ in Ms and Bt age constraints for migmatization along the footwall of the STD through the Lahul valley (between Rhotang pass and Batal) combined with SHRIMP U-Pb in zircon, Ti-in-Bt and Ti-in-quartz thermometry, and thermodynamic modeling from GHS and THS samples provides new constraints for Pressure-Temperature-time-deformation (P-T-t-d) histories for the central Himachal crystalline. Peak metamorphism ~700 °C at 8 kbars near 34 Ma followed by slow extrusion (1-2km/Ma) of GHS migmatites and high-grade gneisses to below 300 °C by ~20 Ma suggest modest exhumation and cooling rates along a late Oligocene to early Miocene STD. Late Oligocene migmatization synonymous with peak metamorphism at shallow and deep structural levels of the GHS suggest anatexis may have facilitated in the extrusion of the GHS through rheologic weakening, similar to other locations in the NW Indian Himalaya. Slow cooling rates (~25-30 °C/Ma), limited duration at peak conditions (~5 Ma), and increasing temperatures with structural level of the GHS favor critical taper models for orogenic development compatible with limited structural disconnect and a broad zone of shear for the STD through Lahul.

I certify that the Abstract is a correct representation of the content of this thesis.

Chair, Thesis Committee

5/25/2016
Date

ACKNOWLEDGEMENTS

My graduate education with the Department of Earth and Climate Sciences has been a challenging and enriching educational experience. It has taught me to think critically and logically, to problem solve, and to be creative. I've grown as a writer and a thinker, and am humbled by the responsibility of contributing to knowledge.

First and foremost, I'd like to thank Mary Leech; for providing the incredible opportunity with her research group. I've had opportunities to travel - literally all over the world; conducting field work in the Indian Himalaya, attending conferences in Vancouver and Baltimore, and conducting lab work at Stanford University, and the University of Vermont. These experiences have broadened my horizons in all fields of geology and introduced me to experts in my field. Mary's resources and guidance through every step of project was essential to completing this study.

I'd like to give a special thanks to my committee members, Jason Gurdak and Karen Grove for their feedback and recommendations. Also Matt Coble at Stanford's SHRIMP lab, Leslie Hayden at the USGS, Dan Jones and Laura Webb at UVM's Noble Gas Lab, and Diana and Clive from SFSU's SEM Lab.

TABLE OF CONTENTS

LIST OF TABLES

LIST OF FIGURES

Figures Page

LIST OF APPENDICES

Appendix Page

1. INTRODUCTION

1.1 Regional Background

The Himalayan-Tibetan orogeny is a type example of a continent-continent collision that is ideal for studying tectonic models to explain ongoing mountain building processes (Dewey and Bird, 1970; Dewey and Burke, 1973; Yin 2006; Kohn, 2014). The northwestern end of the Himalayan belt contains three east-trending, laterally-continuous tectonostratigraphic units separated by two major fault zones (Fig. 1). To the south, low-grade metasediments of the Lesser Himalayan Sequence (LHS) are separated from high-grade crystalline rocks of the Greater Himalayan Sequence (GHS) by the north-dipping Main Central Thrust (MCT). The northern extent of the GHS is separated from overlying low-grade sedimentary rocks of the Tethyan Himalayan Sequence (THS) along the north-dipping South Tibetan Detachment system (STD). The STD and MCT formed to facilitate crustal deformation and extrusion of the GHS after the Indian-Eurasian collision ~50-60 Ma (Leech et al., 2005; Najman et al., 2010). Thermal and mechanical models (channel flow and critical taper) have been developed to explain the post-metamorphic extrusion of the GHS between the LHS and THS along the structural pathways of the MCT and STD (Jamieson et al., 1996; Grujic et al., 1996; Nelson et al., 1996; Unsworth et al., 2005).

The "channel flow" model was developed to explain isothermal P-T paths of high-T/low-P minerals, such as cordierite and spinel (Spear et al., 1999; Ganguly et al., 2000; Groppo et al., 2012, Rubatto et al., 2013; Kohn, 2014). Numerous thermodynamic studies have reinforced and expanded the interpretations of isobaric heating and isothermal exhumation in GHS rocks (Nelson et al., 1996; Beaumont et al., 2001; 2004; Grujic et al., 1996; 2002; Godin et al., 2006; Jamieson et al., 2004; 2006.) According to the model, channel flow is driven by focused denudation from monsoonal rains on the Himalayan range front occurring simultaneously with mid-crustal partial melting and lateral transport of the GHS along a predominately isothermal path. Bright spots on

seismic reflection data (Nelson et al., 1996) and a zone of low resistivity/high conductivity on magnetotelluric data (Unsworth, 2005) have been interpreted as partial melt in the mid crust. This partially-molten middle crust extends beneath southern Tibet, and has been proposed as the source for the lateral channelized flow of the GHS (Hodges, 2000). This channel flow model considers climate as a first order driving force for the structural development of the mountain range.

The critical taper model considers the internal deformation of the orogen to take the form of stacked in-sequence thrusts (Henry et al., 1997; Grasemann et al., 1999; Bollinger et al., 2006; Kohn, 2008; 2014). Once these thrusts form a wedge-like geometry, the system overcomes the angle of internal friction, and the wedge can slide as a whole. The critical taper model involves movement as a series of passive and active roof thrusts along the underlying décollement (MCT). This model assumes a widespread distribution of erosion over the orogen. Although certain areas of the orogeny have experienced extremely rapid exhumation (up to ~40 mm/a), the majority of the orogeny has experienced much slower exhumation rates, on the order of 0.1 to 1.0 mm/a (Kohn, 2014). In the critical taper model, the rate and magnitude of deformation is the primary driving force controlling the structural development of the mountain range, with climate being a less significant factor (Yin, 2006; Kohn, 2014). A similar mechanical model based on general shear (both pure and simple shear), termed the tectonic wedge model (Price, 1986), involves the southwestward extrusion of the GHS as a deformed thrust sheet overlying an undeformed ramp, where alternating top-to-the north and top-to-the south shear senses align well with field observations of ductile shear fabrics (Webb et al., 2007; 2011).

These thermal and mechanical models attempt to explain the emplacement of the GHS based on thermal histories, field and geophysical evidence for melt in the middle crust, the type and amount of slip on the STD and MCT, and the orientations of major structures. These models describe sections of the orogen at different developmental

stages based on the thermal-mechanical state of the system; where the critical wedge model best applies during the cold, rheologically strong, subduction phase and the channel flow best applies during a hot orogenesis phase from continent-continent collision (Jamieson and Beaumont, 2013). Crucial to understanding the tectonic development of the NW Himalayan orogeny is the collection of more data about the location and slip of the STD and MCT. This study focuses on understanding the metamorphic histories of GHS and THS rocks to better constrain the location, timing, and magnitude of slip of the STD through the Lahul valley of the NW Indian Himalaya.

The Lahul valley of NW India is located between two well-defined sections of the STD – the Zanskar shear zone to the northwest and the Sangla detachment to the southeast (Fig. 1). There is controversy about the location and type of shear motion along the STD in the ~50 km strip extending through Lahul valley, where the STD is mapped variably as a discrete fault, a dextral shear zone (CDSZ), or not at all (Vannay and Steck, 1995; Epard and Steck, 2004; Webb et al., 2007; Fig. 2). This study focuses on understanding the pressure-temperature-time-deformation (P-T-t-d) evolution of THS and GHS rocks in Lahul valley to better understand the Cenozoic regional deformation and the location and role of this local segment of the STD in the extrusion of the GHS. Deformed granite, migmatite, and leucogranite from the GHS contain the mineral assemblage Qz + Kfs + Pl + Bt + Ms ± Grt ± Ky, while schists and phyllites from the THS contain the assemblage Qz + Kfs + Pl + Bt + Ms. I calculated isochemical phase equilibria diagrams using *Perple_X*, which utilizes whole-rock chemistry data and solution models based on each rock's mineral assemblages. Ti-in-quartz, Ti-in-biotite, and Fe-Mg exchange thermometry for garnet-biotite pairs, used along with mineral growth relationships, constrain conditions during prograde garnet growth and dominant fabric development during peak and retrograde conditions. I used U-Pb SHRIMP dating of zircon to constrain the age of peak metamorphism and $^{40}Ar/^{39}Ar$ thermochronology of micas to constrain the timing of the cooling history along the valley and across the STD.

This multi-component approach to understanding the metamorphic and deformational evolution of Lahul provides a holistic understanding of the GHS, THS, and STD in a controversial area that can be used to draw comparisons, and build on tectonic models in the NW Himalaya.

1.2 Local Geologic Background

In NW India, the Tethyan Himalayan Sequence (THS) consists of the Cambrian Hiamanta Group and a lower Ordovician-Devonian sequence of shelf sediments. These siliciclastic and carbonate sediments have been intruded in many localities by potassium-rich, megacrystic, Cambro-Ordovician granites and middle Permian volcanics (Dézes, 1999; Webb et al., 2007, 2011, 2013). The GHS is composed of lower-grade amphibolite-facies rocks to high-grade paragneisses and migmatites representing the high-grade core of the orogen (Robyr et al., 2006; Yin, 2006; Webb et al., 2007). Similar to the terminology of Stübner et al., (2014), we use the terms Haimanta metasediments and Deo Tibba granitic gneisses without implication of structural position with respect to the THS or GHS. The gradual transition from low to high grade metamorphism through Lahul valley indicates a gradual transition from GHS to THS; where parts of the Haimanta group and Deo Tibba granitic gneisses may belong to both the GHS and THS.

On a regional scale, the Lahul valley juxtaposes the Shikar Beh Nappe to the southwest and the Nyimaling-Tsarap nappe to the northeast (Dézes, 1999; Steck et al., 1993, 2014; Fig 1). Northeast-vergent thrusting of the Shikar Beh nappe in the Late Eocene-Oligocene produced the NE-vergent Tandi syncline and structural lineations throughout the southern Lahul-Spiti region. Late Oligocene-Early Miocene north Himalayan frontal thrust faults associated with the Nyimaling-Tsarap Nappe are thought to have overprinted NE-vergent structures and metamorphic fabrics with SW-verging nappe-stacking thrust faults, synchronous with high-grade metamorphism and

emplacement of the GHS (Steck et al., 1993a,b; Frank et al., 1973). THERMOCALC (Holland and Powell 1998) modeling of high grade metamorphism near Rhotang Pass indicated peak conditions of 577-584°C at 6.2-6.9 kbars (Walker et al., 1999), and temperatures calculated using Ti-in-biotite thermometry between ~559-636°C (Leger et al., 2013; Fig. 2). Stübner et al. (2014) suggested that discrete episodes of monazite growth at ~36.5 Ma, 30 Ma, and 27 Ma may have corresponded to metamorphism related to these nappe stacking episodes. An alternative model proposed by Singh (2012) asserted that the NE-verging Tandi syncline and SW-vergent Chamba syncline formed during a single deformational event associated with SW-directed thrusting during the Himalayan orogeny. This structure, termed the Hadsar-Chobia box fold, could have formed over the brittle-ductile Chamba thrust sheet above a nearly horizontal décollement during the first deformational episode of the orogeny (Singh, 2012).

Normal shear motion along the STD in the western Himalaya (Zanskar-to-Garhwal) is thought to have begun by at least 23 Ma and ended 11-9 Ma (Dézes et al., 1999; Searle et al., 1999; Walker et al., 1999; Beck et al., in prep; Fig 1), possibly including a large dextral slip component (Yin, 2006). The Zanskar shear zone, interpreted as the western extent of the STD, contains high-grade metasediments of the Haimanta Formation in the footwall and lower grade metasediments of the Haimanta Formation in the hanging wall (Dézes, 1999; Stübner et al., 2014). Near Sarchu, the STD is mapped through Paleozoic to Mesozoic THS rocks in both the footwall and hanging wall along the Sarchu normal fault (Dézes, 1999; Steck, 2003; Stübner et al., 2014). To the east, both the Sangla detachment, and Leo Pargil shear zone contain migmatites in the footwall, with the Sangla detachment containing Paleozoic Deo Tibba intrusives in the hanging wall and the Leo Pargil shear zone containing Paleozoic/Mesozoic THS rocks and unmetamorphosed Haimanta metasedimentary rocks in the hanging wall (Thiede et al., 2006; Stübner et al., 2014). All of these faults zones are in contact, or they are at least in close contact with footwall migmatites described as belonging to the Haimanta

Formation. Similar migmatites are present in the Lahul valley, but occur in the Deo Tibba intrusion, broadly classified as part of the THS. Though Paleozoic intrusive rocks are typically not associated with the metamorphic sediments of the GHS, the Deo Tibba through Lahul regions contain high grade gneisses with index minerals and some migmatization, making these rocks more appropriately grouped with the GHS than THS (Fig. 2).

2. METHODS

2.1 Petrography

Twenty-one GHS and THS rock samples were cut perpendicular to their foliation and parallel to their lineation, and sent to Applied Petrographic Services Inc., where they were sectioned and polished to 1 μm thickness. I produced 15 additional thin sections at San Francisco State University, using a grinding and polishing wheel, to obtain hard-to-find key index minerals and unusual microtextures. Investigating certain microtextures required us to cut thin sections parallel to their foliation; this was done to gain a better three-dimensional understanding of our micro-shear banding in muscovite. We also cut multiple thin sections perpendicular to their foliation and at various angles to their lineation to assess intensities of crenulation cleavage in our micro-shear banded muscovite, to better understand the verging direction of regional deformation. An additional 42 thin sections of rocks from the western Lahul - Rhotang Pass region were provided by Alexander Webb (samples from Webb et al., 2007; Leger et al., 2013) to compare microtextures of our samples with those from surrounding regions.

2.2 Whole Rock XRF

Whole-rock X-ray fluorescence (XRF) and inductively-coupled plasma-mass spectrometry (ICP-MS) analyses were performed at the GeoAnalytical Lab at Washington State University with a Thermo-ARL Advant'XP+ sequential XRF spectrometer and Agilent model 4500 ICP-MS (Tab. 1). Analyses included chipping and grinding of each sample to a very fine powder that was then fused into beads in a muffle oven at 1000° C. After cooling, these beads were reground, chemically treated, and dissolved in de-ionized water for the ICP-MS analysis. For whole-rock XRF, these cooled beads were reground, refused, and polished. The ICP-MS tested for 14 rare earth elements (REEs) and 13 trace elements and the XRF spectrometer tested for 10 major and 19 trace elements.

2.3 SHRIMP U-PB in Zircon

U-Pb depth profiling in zircon was conducted on the sensitive high resolution ion microprobe-reverse geometry (SHRIMP-RG) co-operated by Stanford University and the U.S. Geological Survey (USGS) at the Stanford-USGS Micro Analysis center (SUMAC) from 8/17/15 to 8/19/15 (App. 1). Eight samples were chosen for analysis based on their spatial distribution, lithology, and metamorphic grade. Zircons from three gneisses, two leucogranites, two leucosomes, and one granite were mounted and prepared on site several weeks prior to analysis.

Zircon grains were concentrated by standard heavy mineral separation processes, and individual grains were hand selected and mounted on a glass slide coated with a thin (<10 μms) film of agave nectar. The water soluble agave allows the grains to be easily manipulated and arranged in ca. 1 x 6 mm rows with the flat euhedral zircon {1 0 0} surfaces oriented down against the glass. Oriented zircons grains were pressed into the

pre-polished indium, causing flat non-polished zircon surfaces to be exposed parallel to both the mount surface and standard grains. The indium occupied a 4 mm x 12 mm trough milled into 25.4 mm-diameter aluminum disks. Unknown zircons were co-mounted with ~30 grains of zircon age standard Temora-2 and 3 grains of a compositional standard MADDER, which were polished to ~ 1 μm thickness to ensure a flat surface prior to pressing-in unknowns.

Zircon mounts LV-1 and LV-2 were imaged with plane light on a polarizing microscope at 20x magnification to identify zircons with flat surfaces that are free of inclusions or other phases. The mounts were rinsed with soapy water, followed by a 1N Ethylenediaminetetraacetic acid (EDTA) solution, to remove any surface contamination (particularly Pb). The samples were then thoroughly rinsed in distilled water, dried in a vacuum oven, and coated with gold. The mounts were stored at high pressure (10^{-7} torr) for several hours before being moved into the source chamber of the SHRIMP-RG to minimize degassing of the epoxy and isobaric hydride interferences and masses 204-208.

Secondary ions (positively charged) were sputtered from the target spot using an O_2^- primary ion beam, which was accelerated at 10 kV and had an intensity varying from 2.5 to 3.0 nA. For the analyses performed in this study, the primary ion beam spot had a diameter between 18-20 μm and a depth of ~1 micron. Based on previous analyses of zircons from the nearby Zanskar and Tso Morari terranes (Coble and Leech, 2014; Leech et al., 2014a; 2014b), we expected many of the grains to lack Miocene-age metamorphic rims and to be Paleozoic to Precambrian in age. Therefore, at the beginning of every analysis, we first measured "quick" uncorrected U-Pb ages to avoid analyzing these older grains. The duration of these initial analyses was ~20 seconds, and if the quick $^{206}Pb/^{238}U$ was >0.024 (i.e., >150 Ma), the grain was skipped. If the quick $^{206}Pb/^{238}U$ was <0.024, the sample surface was cleaned by rastering the primary beam for 30 seconds, and the primary and secondary beams were auto-tuned to maximize transmission. The full acquisition routine included analysis of a stoichiometric normalizing species ($^{90}Zr_2{}^{16}O^+$),

followed by $^{180}Hf^{16}O^{+}$, $^{204}Pb^{+}$, a background measured at 0.045 mass units above the $^{204}Pb^{+}$ peak, $^{206}Pb^{+}$, $^{207}Pb^{+}$, $^{208}Pb^{+}$, $^{232}Th^{+}$, $^{238}U^{+}$, $^{232}Th^{16}O^{+}$, and $^{238}U^{16}O^{+}$. All peaks are measured on a single EPT® discrete-dynode electron multiplier operated in pulse counting mode with 7 scans (peak-hopping cycles from mass 196 through 254). Measurements were made at mass resolutions of $M/\Delta M$ = 7800-8500 (10% peak height), which eliminated interfering molecular species, particularly for the REE.

Zircon concentration data for U, Th and Hf were calculated relative to MADDER (3435 ppm U; Barth and Wooden, 2010), which was co-mounted with unknowns on each mount. Calculated model ages for zircon were standardized relative to Temora-2 (416.8 Ma; Black et al., 2004), which were analyzed repeatedly throughout the duration of the analytical session. Data reduction for geochronology followed the methods described by Williams (1997), and Ireland & Williams (2003), and used the MS Excel add-in programs Squid2.51 and Isoplot3.764 of Ken Ludwig (2009; 2012). The measured $^{206}Pb/^{238}U$ was corrected for common Pb using ^{207}Pb, whereas $^{207}Pb/^{206}Pb$ was corrected using ^{204}Pb. The common-Pb correction was based on a model Pb composition from Stacey and Kramers (1975).

The goal of these analyses was to target the thin metamorphic zircons rims that have yielded young ages in several studies throughout the NW Himalaya (Horton and Leech, 2011; Stübner, 2014; Beck et al., in prep). The SHRIMP beam sputter erodes ~1-1.5 μm deep pit, based on measurements by white light interferometry from similar Zanskar samples (Beck et al., in prep), suggesting that it is likely that the analytical pit will sputter through the metamorphic rim before the analysis is complete. Of our 205 analyses, 194 sputtered into Paleozoic to Precambrian age domains in less than 7 cycles, so we infer that the thicknesses of these metamorphic rims are <1.5 μm.

Individual analyses that yielded ages of 23-60 Ma for the first 2 or more cycles, then increased more than ca. 20-500 Ma over the subsequent cycles of data acquisition,

were interpreted to reflect depth profiling into an older age domains. Because the ion-probe pits are generally Gaussian-shaped, the increase in ages reflects mixing between the bottom of the pit and the sides. We reduced the data with only the youngest 3, 5, or 7 cycles (depending on interpretations of sputtering into older age domains) to calculate model ages for the zircon surface-rim ages. U-Pb ages obtained by SIMS were calculated relative to age standard Temora-2, and are reliant upon the assumption that the standards are treated in the same manner as the unknowns. Therefore, the data were reduced using three methods: (1) the U-Pb calibration constant was calculated using 7 cycles of Temora-2 data for unknown analyses that yielded Paleogene ages from 6 or 7 cycles, or (2), unknown sample analyses with 5 scan cycles were run with 5 scan cycle Temora standards, or (3), for analyses which only yielded 2 to 4 cycles of Paleogene ages, the U-Pb calibration constant was calculated using 3 cycles of Temora-2 data.

Of our eight samples, only three had metamorphic rims thick enough to analyze their Cenozoic ages. Several grains from three samples (six from LV-19, three from LV-17, and two from LV-16; App. 1) produced Paleogene ages in accordance with our selection criteria. Data produced by analyses where the beam appeared to have missed the flat grain surface by more than 10% have been omitted. Data with anomalous UO/U ratios (which is sensitive to instrument mass fractionation) or nonradiogenic Pb contamination >8% were also excluded in the final calculations.

2.4 $^{40}Ar/^{39}Ar$ Thermochronology

$^{40}Ar/^{39}Ar$ analyses were performed at the University of Vermont Noble Gas Geochronology Laboratory. Inclusion-free biotite and muscovite mineral grains were handpicked from crushed rock samples under a bioptic microscope after having been washed, sonified, and dried to remove any adhering particulate matter. Grains from each sample were loaded into aluminum foil packets, arranged in a suprasil vial, and placed in

an aluminum canister for irradiation. Samples were irradiated with multigrain aliquots of Fish Canyon Tuff Sanidine to act as a flux monitor (age = 28.03 Ma; Renne et al., 1998) to monitor the neutron dose, and CaF_2 and KSO_4 were also irradiated to determine corrections for interfering nuclear reactions. Samples were irradiated for four hours at the Cadminum-Lined In-Core Irradiation Tube (CLICIT) reactor of Oregon State University in Corvallis, Oregon.

Laser step heating for $^{40}Ar/^{39}Ar$ dating was conducted with a Santa Cruz Laser Microfurnace 75 W diode laser system. Biotite samples were loaded directly into wells in a copper sample holder. Muscovite grains were loaded into degassed Nb foil packets before being loaded into the wells in the sample holder. The gas released during heating was purified with SAES getters and argon isotopes were analyzed on a Nu Instruments Noblesse magnetic sector noble gas mass spectrometer during step-heating analyses. Data from samples and flux monitors were corrected for blanks, mass discrimination, atmospheric argon, neutron-induced interfering isotopes, and the decay of ^{37}Ar and ^{39}Ar. Mass discrimination was calculated by analyzing known aliquots of atmospheric argon for which the measured $^{40}Ar/^{36}Ar$ was compared with an assumed atmospheric value of 298.56 (Lee et al., 2006). Interfering nuclear reactions were corrected for by analyzing argon extracted from irradiated and fused optical grade CaF_2 and KSO_4. Correction factors used to account for interfering nuclear reactions for the irradiated samples are: $(^{40}Ar/^{39}Ar)_K = 8.87 \times 10^{-3} \pm 5.30 \times 10^{-3}$, $(^{36}Ar/^{37}Ar)_{Ca} = 2.7 \times 10^{-4} \pm 0.2 \times 10^{-4}$, $(^{39}Ar/^{37}Ar)_{Ca} = 6.7 \times 10^{-4} \pm 0.2 \times 10^{-4}$. A linear interpolation was used to calculate J factors for samples based on sample position between flux monitor packets in the irradiation tube. All ages were calculated using the isotope decay constants recommended by Steiger and Jäger (1977). The age calculations for inverse isochron and apparent age data were achieved using both an in-house data reduction program and Isoplot 3.0 (Ludwig, 2003).

Weighted mean ages are reported, and plateau ages are reported if sufficient criteria were met (see McDougall and Harrison, 1999). Errors on plateaus and weighted mean ages are quoted at the 1σ level and include precision associated with measurement of the irradiation parameter, J, for flux monitors.

2.5 Electron Microscopy

Major, minor, and trace elements from garnet, biotite, zircon, and quartz were analyzed on a JEOL 8900 electron microprobe at the USGS facility in Menlo on 1/25/2016 through 1/27/2016 to acquire mineral chemistry data for garnet-biotite thermobarometry, and Ti-in-biotite and Ti-in-quartz thermometry. The analyzing conditions were set to 15 kV accelerating voltage with a 15 nA sample current for biotites and garnets, and 15 kV accelerating voltage and 100nA sample current for Ti-in-quartz and Ti-in-zircon analyses. Increased sample current broadened the beam focus from < 1 μm diameter in garnet and biotite analyses, to several microns diameter for quartz and zircon analyses, reducing resolution for targeting zircon rims. Count times for garnet and biotite were 20 s per peak, with a 10 s background for all elements. Count times for Ti-in-zircon and Ti-in-quartz analyses were 40 s per peak, with 10 s background for all elements. Fe^{3+} contents for garnet were estimated using the program AX (Holland, 2009) which recalculated garnets to eight cations per 12 oxygen. For Ti-in-biotite thermometry, biotites were calculated to 22 apfu. Ti-in-zircon data was later omitted due to mixing from poor beam resolution.

Garnet and biotite pairs were calibrated according to Ferry and Spear (1978), with the refinements of Hodges and Spear (1984; Tab. 2), Ganguly and Saxena (1984), and Williams and Grambling (1990). The Hodges and Spear (1984) calibration incorporates non-ideal mixing of Ca, resulting in systematically higher temperatures than from Ferry and Spear (1978). The Ganguly and Saxena (1984) calibration incorporates non-ideal

mixing of Ca (similar to Hodges and Spear, 1984), Mn and the Fe-Mg exchange. The Williams and Grambling (1990) calibration treats Mn, Fe and Mg mixing in garnet independently, specifically intended for high XSps <0.5 and XGrs <0.1. An upper temperature limit was set at ~650°C due to the effects of Ti, Fe^{3+}, Mn, and Al mixing in biotite at higher temperatures.

The Ti-in-biotite thermometer was calculated according to Henry (2005). This thermometer requires biotite compositions of XMg = 0.275-1.0 and Ti =0.04-0.6 apfu, the coexistence of quartz, a Ti-bearing phase (Ilm or Rt), an aluminosilicate, and graphite. Samples in Lahul lack aluminosilicates, however since Al_2O_3 in biotite is high (generally ≥ 18 wt.%), we presume our system is saturated with aluminum; and therefore usable for the thermometer - as in Leger et al. (2013). Results from thermometry are in Tab. 3.

Ti-in-quartz thermobarometry was calibrated according to Thomas et al. (2010), with an $aTiO_2$ of 1, because rutile is a coexisting Ti-bearing phase. Temperatures were calculated across various pressures to form a line on relevant pseudosections, while averaged values were calculated at 6-8 kbar, depending on the sample and textural relationships (Tab. 3; App. 3,-4 for pseudosections). Inclusions of Ti-in-quartz cannot provide information on the temperature during the onset of garnet growth, because quartz was likely present before garnet grew, and is not in equilibrium. Therefore, Ti-in-quartz inclusions in garnet can only be used to estimate the highest temperature at which garnet grew, where the range of values can indicate the thermal range for the metamorphic episode (Storm and Spear, 2009).

2.6 Thermodynamic Modeling using *Perple_X*

Thermodynamic modeling of GHS and THS rocks was done using *Perple_X* computer modeling software (Connolly, 2009). *Perple_X* uses thermodynamic databases

that formulate equations of state, including parameters for enthalpy, entropy, heat capacity and activity for minerals over P-T space. Experimental mineral growth enables researchers to derive solution models containing numerical models to describe mineral growth over changing P-T space in low and high variance phase equilibria. *Perple_X* calculates mineral equilibria over a range of pressures and temperatures, using the unique major elemental composition of each sample and mineral assemblages from petrographic analyses. The program uses free energy minimization for a given mineral assemblage and bulk rock composition, rastering across a cartesian coordinate system of pressure verses temperature. Microtextural analyses link mineral assemblages to deformational episodes, enabling us to connect deformation to modeled P-T paths.

All samples were modeled with thermodynamic components MnO-Na_2O-CaO-K_2O-FeO-MgO-Al_2O_3-SiO_2-TiO_2 (Mn-NCKFMAST) and saturated components H_2O and SiO_2, except for melt models, which do not saturate with H_2O. Thermodynamic data file hp04ver.dat from Holland and Powell (1998) used solution models for garnet (Gt(WPH); White et al., 2000), cordierite ((hCrd); ideal model of Baumgartner, unpublished data, 2003), staurolite (St(HP); Holland and Powell, 1998), chlorite (Chl(HP); Holland et al., 1998), biotite (Bio(TCC); Tajcmanova et al., 2009), muscovite (Mica(CHA); Auzanneau et al., 2010), feldspar (feldspar; Fuhrman & Lindsley, 1988), ilmenite-geikielite-pyrophanite (IlGkPy; ideal), and when appropriate, melt (melt(HP); Holland and Powell, 2001; White et al., 2001). Thermodynamic data file hp11.dat from Holland and Powell (2011) used solution models for garnet (Gt(W); White et al., 2014), cordierite (Crd(W); White et al., 2014), staurolite (St(W); White et al., 2014), chlorite (Chl(W); White et al., 2014), biotite (Bi(W); White et al., 2014), muscovite (Mica(W); White et al., 2014), feldspar ((FspC1(W); White et al., 2014), ilmenite ((Ilm(W): White et al., 2014) and melt (melt(W); White et al., 2014) when appropriate. O_2 was not included as a thermodynamic component due to lack of Fe_2O_3-bearing minerals, and indication that Bt was Fe_2O_3-poor (dark brown colored). The effect of O_2 on the biotite breakdown reaction has been documented as ~50°C greater in KFMASH systems than KFMASHTO

systems (White et al., 2007). Because biotite did not break down, even in our highest grade migmatite, we expect that the influence of O_2 in our samples is insignificant in our modeling regardless if Fe_2O_3 is actually present in a significant quantity. We discuss more effects of O_2 from Fe_2O_3 in the context of *Perple_x* modeling in App. 2.

All samples were modeled in the hp11 thermodynamic database, then re-run in the hp04 database, to better constrain garnet growth. Thermodynamic database file hp11 (Holland and Powell, 2011) is a newer, internally-consistent thermodynamic database developed from the hp04 (Holland and Powell, 1998) database. Many solution models in the hp11 database are either converted from hp04, or are updated versions based on more recently-published thermodynamic data. One of the solution phases in the hp11 database, Chl(W), does not incorporate MnO in the model, which can cause problems with the MnO budget, leading to an effect on garnet stability in coexisting P-T space. Because the hp04 database incorporates MnO in the Chl(HP) solution phase, as well as all other MnO bearing mineral solution phases, I found it appropriate to model garnet stability with the hp04 database instead of hp11 database. Thermodynamic modeling in MnO-bearing and MnO-free systems have shown that the presence or absence of MnO only has ~1% effect on the stability of all mineral phases other than garnet (White et al., 2007; 2014), making our hp11 database preferable for modeling all other phase relations despite the effect of an MnO-free chlorite solution phase. More information about the effect of MnO on garnet stability and thermodynamic modeling can be found in App. 2.

3.0 RESULTS

Temperatures to and from peak conditions were determined in three independent ways. We connected mineral assemblages and textures from thin sections to our pseudosections to constrain stable P-T fields, analyzing compositional zoning profiles of garnets along with conventional thermobarometry to determine prograde and peak temperatures, and applying Ti-in-quartz and Ti-in-biotite thermometry from matrix and

inclusion grains to asses prograde, peak or retrograde conditions based on metamorphic fabric relations. A summary of metamorphism and deformation stages, garnet-biotite thermometry, Ti-in-biotite thermometry, Ti-in-quartz thermometry, and P-T stability from modeling is in Tab. 2, 3 and 4.

3.1 Petrography

A petrographic analysis of the metamorphic and deformational history of Lahul valley rocks is in Tab. 4, with photomicrographs of metamorphic textures in Figs. 3,-4,-5. Studies by Wyss et al. (1999) and Steck et al. (1993) have interpreted metamorphism and deformation through the Lahul region, predominately along a southern transect from the eastern portion of our study area, south of Batal (Fig. 2). Key aspects of our M1/D1 and M2/D2 episodes are not described in these other studies and may be unique to our study area. The best examples of the oldest deformational texture is seen near the center of our study area - in the biotite zone of Deo Tibba gneisses, where mantled porphyroclasts of D2 micro-shear banded Ms1 along with Pl2 porphyroclasts with Ms2 inclusions are preserved within the D3 fabric (Fig. 4a,b). Micro-shear banding of mantled porphyroclasts, used to assess early deformation, become progressively rotated in higher grade samples (Fig. 5c) until they disappear near the garnet zone (Fig. 4d,f). Near the center of our study area (by LV-11; Fig. 2), the D3 fabric is weak enough to preserve the orientation of strain responsible for D2 strain in Ms1. The timing for D2 is poorly constrained, however we can qualitatively reason that prograde deformation records early NNE/SSW to ENE/WSW compression, based on analyses of the changing intensity of micro-shear banding in Ms1 when cut along different strikes. D3 fabric development is recorded in prograde and retrograde assemblages; in both cases near peak conditions ~35 Ma. Progressive deformation, D3, in the migmatites (Fig. 5) occurs as a retrograde fabric near the center of our study area while garnet bearing gneisses in the western section record prograde to peak fabrics. The most exaggerated shear fabrics occur in Haimanta

metasediments, not as a reflection of metamorphic grade, but rather the weak pelitic protolith susceptible to partitioning strain (Fig. 3).

3.2 Haimanta Metasediments

The low metamorphic grade Hiamanta metasediments contain a dominant mineralogy of Qz + Kfs + Pl + Ms ± Bt ± Chl (Fig. 2; 3). They contain better developed S-C and C'–type shear band cleavage than their GHS counterparts, accounting for the best examples of our D3 fabric (Fig 3a,b). They contain no evidence of the D2 micro-shear banding cleavage used to correlate GHS gneisses to the migmatites. Lineations reflecting axial traces fall between 240° to 300° displaying NNW/SSE to NNE/SSW strain, with top-to-the-SE and top-to-the-NW shear sense. No THS samples had zircon rims thick enough to analyze, but we assume peak metamorphism in these samples occurred as the same time as higher-grade samples to the west (Fig. 2).

Chlorite zone: Sample LV-10

Chlorite schist LV-10 was taken from the southern end of the Shigri fold along the westernmost contact of the STD transecting Lahul, containing the assemblage Ms + Qz + Kfs + Pl + Chl + Rt + Ttn (Fig. 2). The Shigri fold includes isoclinal folding, box folding, and well developed thrust contacts (Kumar and Dobhal, 1997; Wyss et al., 1999; Sharma et al., 2013). This sample reflects a transition from right way up metamorphism to inverted metamorphism, where samples increase in metamorphic grade to biotite conditions to the east (Fig. 2). The sample is predominately composed of a green mica, probably phlogopite; as corroborated by the high MnO content. Chlorite mostly occurs as a retrograde texture overprinting, or mimicking, the D3 foliated muscovite.

Biotite zone: Samples LV-8, -9

Slate LV- 8 was taken from the northernmost Haimanta group along the STD contact, containing a well-defined S-C fabric and an assemblage Qz + Kfs + Pl +Ms + Bt

+ Chl + Ilm + Rt + Ttn (Fig. 2; 3b). Slate LV-9 was taken south of LV-8 along another section of the STD within the Haimanta formation, along the eastern limb of the Shigri fold. Brown, fine grained biotites show intense heating effects suggesting periodic reheating of Deo Tibba gneisses below (Rawat and Purohit, 1988; Sharma et al., and Pottakkal, 2013; Fig. 3a). This slate has a better developed S-C and C' type shear band cleavage than LV-8, and GHS counterparts of similar metamorphic gradae - containing the assemblage Qz + Kfs + Pl + Bt + Rt. Thin sections cut perpendicular to the foliation and parallel to the fold axis/crenulation cleavage show top-to-the NW and top-to-the SE shear sense.

3.3 Deo Tibba Gneisses and Migmatites

The metamorphic index mineral in Deo Tibba gneisses changes from chlorite and biotite grade in the east, to kyanite grade in the west, followed by a decrease to garnet grade (Fig. 2). Metamorphic grade increases moving from east to west along the valley due to structural deepening from the antiformal shape of the GHS. Top-to-the-NE and top-to-the-SW shear indicators are present on outcrop and thin section scales, consistent with observations by Jain et al. (1999) and Webb et al. (2007)(Fig. 4). Ms1 can be identified in weakly deformed, THS, Cambro–Ordovician granitic gneisses all the way to migmatic samples within the GHS, making them unique minerals for microtextural correlation, and one of the oldest recorded microtextures in the NW Himalaya (Fig. 4a,b; Fig 5a,b,c,e).

Chlorite zone: Samples LV-1, -2

These granites are very weakly foliated with poorly-developed, to no shear fabric and an assemblage Qz + Pl + Ms + Rt + Ttn + Ilm + Chl (Fig. 2). Coarse grained undulous quartz, and large mantle porphyroclasts of feldspar and muscovite inclusions occur along the 90/90 cleavage planes. Muscovite porphyroclasts resemble micro-shear banding in

M1 muscovite samples from higher grade rocks, but lack shear-banding intensity and uniformity in orientation caused by substantial D2 deformation.

Biotite zone*: *Samples LV-11, -12, -4

Gneisses LV-11 & 12 were collected just outside the migmatite zone, containing the assemblage Qz + Pl + Ms + Bt + Rt + Ttn (Fig. 2; 4a-b). Micro-shear banding of muscovite in these samples can be compared to the micro-shear banding in muscovite of leucosome LV-14 (Fig. 5) and low grade gneisses LV-2 & 7. This sample is sufficiently low grade so that mantled porphyroclasts of muscovite didn't undergo significant reorientation after D2 deformation, making them ideal for understanding prograde regional strain.

Leucogranite LV-4 was taken from a weakly foliated leucogranite dike cross cutting the Deo Tibba Gneisses in the Biotite zone (Fig. 2). It contains the assemblage Qz + Pl + Kfs + Ms with a trace of Bt + Ttn + Ilm. Zircon rims from leucogranite LV-4 produced young quick scan ages, as young as 25 Ma, however rims were significantly thinner than 1 μm, so we couldn't run a full 7 scan analysis on the SHRIMP without sputtering into Paleozoic age domains. Cross-cutting relationships indicate emplacement after the dominant D3 fabric development. Through geochemical comparisons from other GHS leucogranites in the NW Himalaya, we can correlate the chemistry of our leucogranite to tectonic events and melt mechanisms for the region. According to the geochemical classification for tectonic discrimination diagrams presented by Pearce et al., (1984), this leucogranite is classified as a syncollisional granite, with Nb + Y vs Rb large ion lithophile elements in similar quantities to the GHS leucogranite compositions reported by Dézes (1999), Dietrich and Ganser (1981), and Scaillet et al. (1990). Leucogranites from Zanskar, Gumburanjun and Manaslu have comparable major elemental abundances to leucogranites in Lahul (Dézes, 1999).

Large ion lithophile element covariation from leucogranites in the NW Himalaya have been used to estimate the mechanism and percent of partial melting necessary for

leucogranite production and emplacement. Work by Harris and Inger (1992), Inger and Harris (1993) and Harris et al. (1995) show a connection between changing geochemistry and mineralogy in leucogranites as a consequence of different mica melt reactions: vapor absent biotite melting, vapor saturated muscovite melting, or vapor absent muscovite melting. Our leucogranite chemistry, plotted with data from Zanskar (Herren, 1987; Dézes, 1999) show an increase in Rb/Sr accompanied by a decrease of Ba and Sr. This suggests that vapor absent breakdown of muscovite occurred through dehydration reactions with a relatively small degree of partial melt (F=~12%) (Dézes, 1999).

Garnet zone: Samples LV-17, -19

Garnet-bearing gneisses are the highest grade samples we collected for whole rock analysis from the Deo Tibba, containing the mineralogy Grt + Qz + Fsp + Ms + Bt + Rt + Ttn. Garnet porphyroclasts occur as inclusion-rich and inclusion-poor, ranging in size from ~1 mm – 0.01 mm. Electron microprobe transects of garnet from core to rim show subtle prograde zoning in $Alm_{55(core)-63(rim)}$, $Sps_{34(core)-27(rim)}$, $Grs_{5(rim)-1(core)}$, and $Prp_{3(rim)-1(core)}$ (Fig. 6b). LV-19 garnet zoning shows a different prograde pattern, either due to partial garnet reabsorption, or complex zoning, where $Alm_{60(core)-55(inner\ rim)-59(outer\ rim)}$, $Sps_{32(core)-36(inner\ rim)-31(outer\ rim)}$, $Grs_{08(outer\ rim)}$, $_{08(inner\ rim)-07(core)}$, and $Prp_{01(outer\ rim)-01(inner\ rim)-01(core)}$(Fig. 6a). Values were acquired at their lowest Mn value prior to any slight reversal in zoning due to reabsorption at the outer rims. Retrograde net transfer reactions are not likely a concern due to continuous Mn and Fe# (Fe/(Fe + Mg)) decrease from core to rim, with little or no Mn or Fe# reversal (Kohn and Spear, 2000; Fig. 6b). These values suggest a decrease in temperature from the core to inner rim, followed by an increase in temperature from the inner rim to the outer rim, as calculated by conventional thermobarometry (Tab. 2). Ti-in-biotite thermometry of an inclusion in Grt also suggests a cooling trend as Grt was growing from core to inner rim (App. 3b). Similarly matrix Ti-in-biotite from LV-17 and LV-19 show temperature increasing in the M3 matrix biotite, which could indicate a warming trend during inner rim to outer rim growth.

Ti-in-quartz and Ti-in-biotite from garnet inclusions constrain prograde through peak garnet growth (Tab. 3). Increasing temperatures during M3/D3 matrix biotite growth indicates that the dominate fabric grew during prograde to peak conditions, between ~620-675°C. Garnet transects show subtle variations in cation proportions, either indicating a degree of cation re-absorption near peak conditions, or that garnet growth caused little to no cation sequestration, leading to steady absorption Fe-, Mg-, Mn-, Ca. Since garnet occurs in such low modal abundance, and exhibits limited zoning, we didn't make any adjustments to bulk rock compositions in our modeling to accommodate changing bulk rock composition.

Kyanite zone: near Sample LV-18

This sample is a highly foliated gneiss taken next to a kyanite bearing quartz vein (Fig. 2). The sample itself contains the mineralogy Fsp + Ms + Bt + Rt + Ttn though lies in the garnet/kyanite field (Fig. 4e). The shift from kyanite to garnet grade index minerals may not be an accurate representation of the true metamorphic conditions. The kyanite found near LV-18 was in a biotite rich quartz vein cross-cutting the foliation of the local Deo Tibba gneiss. We believe the felsic bulk rock composition of the Deo Tibba is the probable inhibiting factor for the growth of Ky (and garnet). Our samples contain extremely low modal abundances of both garnet and no Ky, which is also supported by low predicted modal percentages from our thermodynamic modeling.

Migmatites: *Samples LV-13, 14, 15, 16*

Melanosome LV-13 contains highly corroded Ms1, with an assemblage Bt + Ms + Fsp + Qz + Tur + Rt, while leucosome LV-14 contains mostly An + Ab, with trace amounts of Ms + Bt + Qz + Tur + Rt and little to no corrosion of Ms1 (Fig. 2; 5). Migmatites are predominately products of in situ partial melting without much evidence for melt migration. Ti-in-quartz thermometry of recrystallized quartz melt within

corroded Ms1 (Fig. 5a-c) and Ti-in-biotite thermometry produce minimum temperature estimates ~620-700°C, within the range of vapor present melting for the assemblage Ms + Pl + Qz (Spear, 2003; Leger et al., 2013; Tab. 3) or dehydration melting for the assemblage Ms +Ab + Qz (Peto, 1976). Rt filled transgranular microfractures above and below mantled porphyroclasts of Ms1 in the melanosome contain no evidence of melt, so we cannot infer the former existence of melt-filled cracks (Sawyer, 2001; Fig 5a); however microfractures can indicates high dilational strain at or near peak conditions, associated with volume change due to muscovite dehydration and melt production. Studies have shown that biotite dehydration causes small positive to large negative dilational strain, while muscovite produces large positive dilational strain capable of generating abundant fractures (Sawyer, 2001). Since the production of melt may depend on the breakdown of muscovite, and the leucosome contains little evidence of dehydration melting in Ms1, melt production likely occurred in a low modal % prior to melt segregation. A lack of transgranular microfractures in the leucosome is consistent with a lack of melt production within the leucosome, seen by the preservation of Ms1, with little to no evidence of dehydration. Since melt segregation is not entirely dependent on fracturing; melt segregation occurs even if the strain produced by volume change through dehydration is small, providing a mechanism for the segregation of melt without producing microfractures in the leucosome.

Sample LV-16 is the highest grade migmatite with the assemblage Grt + Bt + Ms + Fsp + Qz + Tur + Rt. Biotite and muscovite form the dominate M3/D3 matrix foliation but there is no evidence of Ms1, nor corrosion in any muscovite. This sample either reached higher temperatures than LV-13-14-15, or spent a greater amount of time at similar P-T conditions that allowed for the complete breakdown of Ms1, making our M3/D3 fabric a slightly retrogressed assemblage. This could mean that temperatures were in excess of 700°C in the central to western section of the valley.

3.4 Pseudosection Modeling

P-T paths from Deo Tibba gneisses and Haimanta metasediments are located in Fig. 7, with individual pseudosections in App. 3 & 4. Prograde P-T paths are constrained by a lack of Zo growth as an upper limit, peak conditions are constrained by garnet or biotite fields, and retrograde conditions are constrained by lack of aluminosilicate growth.

Peak P-T estimates of our highest grade Grt bearing samples, LV-17 and LV-19 are based on contouring core and rim garnet microprobe compositions as isopleths for XMn and XFe on our pseudosections (See App. 3). LV-17 garnets have zoning in $Alm_{55(core)-63(rim)}$, $Sps_{34(core)-27(rim)}$, $Grs_{05(rim)-1(core)}$, and $Prp_{03(rim)-01(core)}$ suggesting a peak stability of 5.5 - 8.5 kbar at ~650-700°C. Garnet compositions in LV-19 of $Alm_{60(core)-55(inner\ rim)-59(outer\ rim)}$, $Sps_{32(core)-36(inner\ rim)-31(outer\ rim)}$, $Grs_{08(outer\ rim)-08(inner\ rim)-07(core)}$, and $Prp_{01(outer\ rim)-01(inner\ rim)-01(core)}$ suggest a similar peak stability of ~5-9 kbar at 625-675 °C. Contoured isopleths suggest an ~25°C decrease in temperature from core to inner rim compositions, followed by a ~25°C increase in temperatures from inner rim to outer rim. Similar Ti-in-biotite zoning from a biotite inclusion between the core and inner garnet rim suggest ~14°C temperature decrease from 621-607°C, while matrix biotite from M3/D3 fabric development during peak conditions suggest ~60°C temperature increase from ~610-670°C. Since the Ti-in-biotite thermometer also relies on the XMg in bioitite, which can be sensitive to cation exchange within garnet, we checked that the XMg was not zoned in our biotite. The Ti-in-biotite thermometer serves as an independent constraint on temperature decrease followed by temperature increase during garnet growth in LV-19. Ti-in-quartz averages of growth during peak conditions in GBM fabrics for LV-17 and 19 are 630±70°C and 636±40°C respectively. Retrograde conditions from garnet grade samples are constrained by aluminosilicate growth as a lower pressure boundary, restricting P-T paths from complete isothermal decompression.

Deo Tibba biotite grade samples LV-11 and LV-7 are separated by multiple potential segments of the STD, yet show similar peak P-T estimates to each other, and to Grt bearing samples to the west, with maximum P-T stability fields of ~3.6-9.0 kbar at

620-680°C. Even though these samples contain lower grade index minerals, modeling predicts that their more felsic bulk rock compositions could place them in P-T space similar to samples with higher grade index minerals.

Haimanta group biotite grade samples LV-8 and LV-9 have peak P-T fields of 3.4-7 kbar at 475-580 °C, with upper limits constrained by Grt assemblages. These conditions are considerably lower pressure and temperature than biotite grade samples modeled from the Deo Tibba. Work by Wyss et al. (1999) suggested that the THS near LV-8 and LV-9 contains garnet, however, we did not see garnet in the field, or in thin section. If garnet is present, our P-T estimates would be much closer to paths predicted in our biotite grade Deo Tibba gneisses. Ti-in-biotite and Ti-in-quartz from LV-8 provide temperature estimates of ~667°C and 599°C, respectively. These estimates reflect a 20°C-100°C discrepancy between pseudosection modeling and thermometry.

Deo Tibba gneiss LV-2 and Haimanta group schist LV-10 are chlorite grade samples with similar maximum P-T constraints between <1-3.6 kbar and 475-580°C. The upper P-T limit of these samples is constrained by the biotite isograd. Microtextural relations indicate that these samples record the highest metamorphic grade attained rather than retrogressed conditions from a higher grade metamorphic assemblage.

3.5 U-Pb in Zircon Dating

Eight samples were chosen for analysis based on spatial distribution, lithology, and metamorphic grade, however, only three had metamorphic rims thick enough to analyze their Cenozoic ages. From these three samples (LV-19, LV-17, and LV-16), 6, 3, and 2 grains per sample produced Paleogene ages, in accordance with our selection criteria (Fig. 8a-c; App. 1). Garnet grade gneiss LV-19 produced a weighted average mean age of 34.7±1.4 Ma and intercept age of 34.8±1.3 Ma., with individual analyses ranging from 33.6–38 Ma and Th/U ratios between 0.022 and 0.029. Garnet grade gneiss LV-17 produced a weighted average mean age of 34.5±5.9 Ma and intercept age of 34.8±5.3 Ma., with individual analyses ranging from 29.8–35.3 Ma and Th/U ratios

between 0.014-0.016. Migmatite LV-16 produced a weighted average mean age of 34.0±17 Ma and intercept age of 34.5±1.5 Ma., with individual analyses of 33.1 and 35.7 Ma and Th/U ratios of 0.006 and 0.008. Similar ages of 35.8±1.3 Ma and 28.9±0.7 Ma of the central Himachal crystalline have been reported by Stübner et al. (2014). Ti-in-zircon thermometry of Stübner et al.'s (2014) samples suggested zircon overgrowths occurred between ca. ~650-700°C. This is consistent with peak temperature constraints by Ti-in-quartz and Ti-in-biotite thermometry from this study.

Migmatic sample LV-16 shows the lowest Th/U ratios in zircon— 0.006 and 0.008—followed by twice the values for metamorphic zircons in LV-17— 0.014-0.016— and four times the values for metamorphic zircons in LV-19—0.022 and 0.029. The distribution of values varies linearly with geographic distribution rather than metamorphic vs magmatitic zircons. Grain morphology of metamorphic or magmatic rims is difficult to decipher based on <1 μm overgrowth rims on 100-200 μm euhedral to metamorphic zircon grains. Cross cutting relationships in the field, as well as microtextural analyses suggest migmatitic samples are related to the Himalayan migmatization rather than an Ordovician event overprinted with metamorphic zircon growth.

3.6 $^{40}Ar/^{39}Ar$ Thermochronology

Timing for the onset of exhumation is constrained by $^{40}Ar/^{39}Ar$ in Ms and $^{40}Ar/^{39}Ar$ in Bt thermochronology (Fig. 9a-c). The oldest age occurs in migmatite LV-16, which experienced a biotite plateau age of 30.11±0.21 Ma and a muscovite age of 18.4±0.14 Ma. Biotite grade sample LV-11 produced a step heating age of ~27 Ma (data still being acquired), and garnet grade gneiss LV-19 produced a step heating age of 20.84±0.16 Ma. The youngest ages (~21 Ma) are from the garnet/kyanite grade sections and migmatite zone (~18 Ma), followed by a slight decrease in age in the Bt zone (27 Ma) and a dramatic increase in age crossing more segments of the STD through the chlorite zone (~60 Ma, Stübner et al., 2014). Younger ages in the central and western

sections of the valley are most similar to previous studies for the central Himachal crystalline (Schlup et al., 2011; Stübner et al., 2014), reflecting higher grade conditions for a longer duration of time at deeper structural levels. Older ages in the western section of the valley didn't reach the same peak conditions as the higher grade gneisses and migmatites to the west, so their ages reflect shallower structural depths. Migmatite LV-16 likely records multiple generations of Bt growth, seen by an irregular step heating profile, and ~10 ma older than expected age. West of Rhotang Pass, a biotite age of 43.1±0.4 Ma is thought to be related to metamorphism during the Shikar Beh nappe-forming event (Schlup et al., 2011). Similarly, the 30 Ma $^{40}Ar/^{39}Ar$ in Bt age from LV-16 may be a result from inheritance and/or mixing from mica grains related to this early nappe stacking event.

Calibration of Tc (closure temperature) in the $^{40}Ar/^{39}Ar$ in Ms system varies between ~300 to 480°C in similar regional studies of the NW Himalaya (Chambers et al., 2009; Schlup et al., 2011). This study assumes a 400°C closure temperature for muscovite and 300°C closure temperature for biotite, similar to upper constraints of Tc used by Stübner et al., (2014).

3.7 P-T-t-d Histories

New thermometry, thermodynamic modeling, U-Pb in zircon and $^{40}Ar/^{39}Ar$ in muscovite and biotite enables us to quantify burial history and exhumation of Deo Tibba gneisses and Haimanta metasediments across the STD through Lahul valley in four main stages (Fig. 7).

Stage 1 occurs from prograde to peak metamorphic conditions, recognized elsewhere in the central Himachal crystalline by mineralization of monazite from ~41-36 Ma due to crustal thickening (Stübner et al., 2014). Prograde NNE/SSW to ENE/WSW compression (D2) recorded in our oldest GHS microtexture Ms1 can be correlated back to weakly-deformed Chl-grade granitic gneisses in the STD hanging wall. Syn-post D2 deformation

recognized by Pl2 growth with bi-directional Ms2 inclusions may be from a relict shear fabric during progressive prograde metamorphism from early nappe stacking episodes (NE-vergent Shikar Beh and SW-vergent Nyimaling nappes). Evidence of these episodes is structurally present in the eastern section of the valley (Steck et al., 1993; Wyss et al., 1999), however we do not have any distinct U-Pb in zircon age clusters suggesting multiple heating events within the valley and placing these microtextures at prograde P-T conditions.

Stage 2 occurs at peak conditions, constrained by U-Pb in zircon depth profiling near ~35 Ma.. SW directed folding and thrusting coincident with the southwest vergent crystalline nappe emplacement created M3/D3 fabric development throughout the valley. Thrusting in the Shigri fold and inverted metamorphism in duplex structures in eastern Lahul are likely caused by southwest vergent isoclinal folding and thrusting (Rawat and Purohit, 1988; Wyss et al., 1999; Sharma et al., 2013; this study). The 60 Ma $^{40}Ar/^{39}Ar$ in Ms age by Stübner (2014) indicates that samples in the eastern section of the valley were never reset past the closure temperature during the peak metamorphic conditions ~35 Ma, suggesting lower temperatures during the onset of exhumation caused by a shallower structural depth.

A hiatus at or near peak conditions is difficult to constrain without monazite analyses. Stages of monazite crystallization as young as 26 Ma (Stübner et al., 2014) from structurally deeper sections of the central Himachal crystalline suggest a ~10 Ma hiatus near peak conditions. Residence time at peak conditions is responsible for differences in microtextural development, since modeling and thermometry constrain similar peak temperatures along the GHS through the valley. In migmatites, structurally shallow samples show evidence for melting of Ms1 (melt pockets of Qz), and structurally deeper samples show complete dissolution of mantled porphyroclasts of Ms1. As we would expect, structurally deeper samples experienced a longer duration near peak conditions. Further monazite thermochronology could better constrain the duration of

high-grade metamorphism in relation to structural level and STD proximity within the valley.

Stage 3 occurs from peak metamorphism through isothermal decompression and exhumation through the $^{40}Ar/^{39}Ar$ in Ms and Bt closure temperatures, where all Deo Tibba gneisses and the leucosome experience similar P-T paths. It's possible that zircon growth continued from peak conditions through nearly isothermal decompression from 700°C near 8.5 kbar to ~650°C near 5.5 kbar. If this is the case, nearly isothermal decompression may have exhumed migmatite LV-16 and gneiss LV-19 from ~28 km to 18.5 km depth with only ~50°C cooling before crossing the closure temperature for zircon mineralization (~700-650°C, as determined by Stübner et al. (2014) on similar Oligocene overgrowths). From 5.5 kbar at ~650°C, gneiss LV-19 was exhumed to ~5 km depth by 21 Ma at a rate of ~1 km/Ma.

Assuming the 35 Ma zircon age represents the peak metamorphic pressure and temperature, ~8.5 kbar at 700°C, at a depth of ~28 km, then isothermal decompression from 8.5 kbar to 5.5 kbar would have occurred ~2 km/Ma, with similar exhumation rates down to 1.5 kbar through the $^{40}Ar/^{39}Ar$ closure temperatures in muscovite and biotite. Late stage monazite growth ~26 Ma found elsewhere in the central Himachal GHS have been used to quantify a hiatus at peak conditions, and produce significantly more rapid exhumation rates when calculated with similar $^{40}Ar/^{39}Ar$ in Ms and Bt dates.

Stage 4 occurs from the $^{40}Ar/^{39}Ar$ in Ms and Bt closure temperatures through final exhumation to the surface, with slow exhumation rates ~0.3 km/Ma and very slow cooling rates ~15°C/Ma.

4.0 APPLICATIONS AND DISCUSSIONS

Exhumation and cooling rates are highly sensitive to our interpretations of the duration at peak conditions. U-Pb in zircon analyses produced only late Eocene to early

Oligocene ages in Lahul valley, whereas monazite geochronology and U-Pb in zircon ages from deeper structural levels in the central Himachal crystalline constrain peak conditions as late as 26 Ma (Stübner et al., 2014). Depth profiling of U-Pb in zircon produced no individual scan ages younger than ~33 Ma, indicating 1) an earlier onset of exhumation for shallower structural levels of the GHS than elsewhere in the central Himachal crystalline, or 2) earlier onset of cooling from peak conditions due to shallow structural level, or 3) there is a young age signature for peak conditions not captured in the scope of this study (26 Ma; Stübner et al., 2014). If the latter is true, monazite geochronology throughout the Lahul valley could better constrain the onset of exhumation for the GHS, leading to more accurate cooling and exhumation rates along the STD.

Monazite growth constrains the onset of prograde Barrovian metamorphism ~41 Ma (Stübner et al., 2014) to peak conditions determined in this study by ~35-33 Ma. Moderate cooling rates of ~24-27°C/Ma from peak conditions (700°C) through the $^{40}Ar/^{39}Ar$ muscovite and biotite closure temperatures (400°C and 300°C respectively) are significantly lower than other regional studies of the central Himachal crystalline; ~60°C /Ma (Schlup et al., 2011; Stübner et al., 2014). Oligocene–Pliocene cooling rates of ~16±4°C/Ma to Quaternary rates of ~32±2°C/Ma (Yin, 2006) near Zanskar compare well with our results. Cooling rates remain nearly identical from peak conditions ~34 Ma through the muscovite and biotite closure temperatures, then reduce to very slow rates (~15°C /Ma) after ~18-20 Ma, based on correlating zircon and apatite fission track dates from Schlup et al. (2011) (Fig. 10). This may place broad constraints on motion along the STD through Lahul to between <35 Ma and >18 Ma, at which point exhumation and cooling drastically slowed.

In eastern Lahul exhumation rates from peak conditions are poorly constrained due to broad peak P-T fields predicted by modeling, few thermometry analyses and limited thermochronologic data. Significantly older $^{40}Ar/^{39}Ar$ in Ms ages (60 Ma) near LV-2-7 indicate lower temperatures at shallow crustal levels during the emplacement of

the crystalline nappe through the valley. Chlorite through biotite grade inverted metamorphism north of the STD, in Haimanta schists and slates, and again in Deo Tibba granitic gneisses require southwest vergent folding and thrusting, which was likely occurring prior to or synchronous with emplacement of the crystalline nappe (Vannay and Steck, 1995). Isoclinal folding and thrusting has been mapped throughout this area by various authors (Kumar and Dobhal, 1997; Wyss et al., 1999; Sharma et al., 2013), however, a refinement of structural analyses and metamorphic isograds are necessary to better understand what tectonic stage is reflected in the eastern section of the valley.

Structural data and unit correlation have been important to the development of tectonic models explaining the extrusion of the GHS in the NW Himalaya. The structure of the NW Himalaya generally consists of stacked recumbent folds. The central Himachal crystalline belt through Lahul belongs to the Phojil recumbent fold anticline. Tectonic models explaining the emplacement of this structure vary, either occurring as a late stage incidental structure (Webb et al., 2007; 2011), or forming after the D3 foliation, where progressive thrusting folded Barrovian isograds (Epard et al., 1995; White et al., 2008). A key difference in these models is based on differing interpretations of the underlying geometry and classification for lithotectonic units used to determine the location of the MCT, which has been mapped at the foot of Rhotang Pass (Thakur, 1992; White et al., 2008; Figure 1) or ~60 Km to the southwest near the Mandi thrust (Webb et al., 2007, 2011). Structural interpretations based on a MCT near the Mandi thrust led to the tectonic wedging model (derived by Price, 1986; advocated for application in the NW Himalaya by Webb et al. 2007; 2011) to explain top-to-the N and top-to-the S shear indicators present throughout Lahul. This model involves an undeformed ramp and deforming roof thrust that records alternating slip along the STD. The modified channel flow model by Beaumont et al. (2004) predicts that asymmetric thrust extrusion along the STD allows for normal and reverse shear, correlating to-top-the north and top-to-the south shear sense indicators as well.

In this study, thermodynamic modeling, thermometry, and thermochronology have enabled us to compare orogenic models based on their timing of near peak conditions, amount of slip along the STD, and cooling and exhumation histories (similar approach as Kohn, 2008; Tab. 5). U-Pb in zircon geochronology produced a 0.8 Ma range in age for three high grade GHS samples at peak conditions (34-34.8 Ma) suggesting high grade metamorphism occurred simultaneously throughout the valley in a short period of time. This limited residence time of ~1 Ma is mostly consistent with predictions of limited peak conditions from critical taper models (peak conditions ~5 Ma; Kohn, 2008). Critical taper models predict an increase in temperature structurally upward toward the STD, as seen by slightly higher thermometry temperatures throughout the Lahul valley GHS (587-692°C, upper structural level) than those reported in the GHS near Rhotang (560-670°C, lower structural level) (Leger et al., 2013). Additionally, moderate GHS cooling rates from peak conditions ~25-30°C/Ma are similar to critical taper rates of 40-45°C/Ma. Clockwise P-T paths show slight isothermal decompression followed by moderate cooling and decompression, non-ideally fitting aspects of both critical taper (Henry et al., 1997; Bollinger et al., 2006) and channel flow models (Jamieson et al., 2004). While P-T-t-d estimates fit neither model perfectly, samples draw closer comparisons with the mechanically driven critical taper model than the thermally driven channel flow model.

Little structural disconnect along the STD and previously limited evidence for rheologic weakening through partial melting has suggested a harder rheology in the central Himachal than elsewhere in the NW Himalaya. Structural features and deformation through this region is thought to represent a style of deformation that the entire GHS may have underwent in the Eocene to Oligocene prior to the SW extrusion of the GHS (Stübner et al., 2014). Similar U-Pb in zircon ages between migmatites and gneisses indicate that peak metamorphism and widespread partial melting through Lahul were occurring at the same time. Late Oligocene migmatization synchronous with peak metamorphism at shallow and deep structural levels of the GHS suggest anatexis may

have facilitated the extrusion of the GHS through rheologic weakening, similar to other locations in the NW Indian Himalaya. Near identical cooling and exhumation rates between migmatites and high grade gneisses from peak conditions indicate exhumation occurred with no structural disconnect, a result supported by field observations of in situ migmatization, with a lack of melt escape networks. Little field evidence for faulting and similarities between cooling histories for GHS samples support a broad STD with limited discrete disconnect most consistent with P-T-t-d predictions for mechanically driven orogenic development.

REFERENCES CITED

Auzanneau, E., Schmidt, M.W., Vielzeuf, D. and Connolly, J.A.D., 2010, Titanium in phengite: a geobarometer for high temperature eclogites: Contributions to Mineralogy and Petrology, v. 159, p. 1–24.

Barth, A.P., and Wooden, J.L., 2010, Coupled elemental and isotopic analyses of polygenetic zircons from granitic rocks by ion microprobe, with implications for melt evolution and the source of granitic magmas: Chemical Geology, v. 277, p. 149–159.

Beaumont, C., Jamieson, R.A., Nguyen, M.H., and Lee, B., 2001, Himalayan tectonics explained by extrusion of a low-viscosity crustal channel coupled to focused surface denudation: Nature, v. 414, p. 738–742, doi: 10.1038/414738a.

Beaumont, C., Jamieson, R.A., Nguyen, M.H., and Medvedev, S., 2004, Crustal channel flows: 1. Numerical models with applications to the tectonics of the Himalayan-Tibetan orogen: Himalayan-Tibetan Crustal Channel Flows: Journal of Geophysical Research: Solid Earth, v. 109, doi: 10.1029/2003JB002809.

Black, L.P., Kamo, S.L., Allen, C.M., Davis, D.W., Aleinikoff, J.N., Valley, J.W., Mundil, R., Campbell, I.H., Korsch, R.J., Williams, I.S., and Foudoulis, C., 2004, Improved $^{206}Pb/^{238}U$ microprobe geochronology by the monitoring of a trace-element-related matrix effect; SHRIMP, ID–TIMS, ELA–ICP–MS and oxygen isotope documentation for a series of zircon standards: Chemical Geology, v. 205, p. 115–140, doi: http://dx.doi.org/10.1016/j.chemgeo.2004.01.003.

Bollinger, L., Henry, P., and Avouac, J., 2006, Mountain building in the Nepal Himalaya: Thermal and kinematic model: Earth and Planetary Science Letters, v. 244, p. 58–71, doi: 10.1016/j.epsl.2006.01.045.

Coble, M.A. and Leech, M.L., 2014, Resolving the youngest episode of zircon rim growth with high-spatial resolution SIMS: U-Pb ages and trace element analyses from <1 μm thick metamorphic zircon rims from the Zanskar Shear Zone and Tso Morari UHP Complex, NW Himalaya, Eos Trans., Am. Geophys. Union, Fall Meeting Supplement, Abstract V34A-05.

Connolly, J.A.D., 2009, The geodynamic equation of state: What and how: Geodynamic Equation of State-What and How: Geochemistry, Geophysics, Geosystems, v. 10, doi: 10.1029/2009GC002540.

Dewey, J.F., Bird, J.M., 1970, Mountain belts and new global tectonics: Journal of Geophysical Research, v. 75, p. 2625 – 2685

Dewey, J.F., Burke, K., 1973, Tibetan, Variscan and Precambrian basement reactivation, products of continental collision: Journal of Geology, v. 81, p. 683 – 692.

Dèzes, P.J., Vannay, J.C., Steck, A., Bussy, F., Cosca, M., 1999, Synorogenic extension: quantitative constraints on the age and displacement of the Zanskar shear zone (northwest Himalaya): Geological Society of America, Bulletin 111, p. 364–374.

Dietrich V., Gansser A., 1981, The leucogranites of the Bhutan Himalaya (crustal anatexis versus mantle melting): Schweiz. Mineral. Petrogr. Mitt., v. 61, no. 2-3, p. 177-202.

Epard, J.-L., and Steck, A., 2004, The Eastern prolongation of the Zanskar Shear Zone (Western Himalaya): Eclogae Geologicae Helvetiae, v. 97, p. 193–212, doi: 10.1007/s00015-004-1116-7.

Ferry, J. t, and Spear, F.S., 1978, Experimental calibration of the partitioning of Fe and Mg

between biotite and garnet: Contributions to mineralogy and petrology, v. 66, p. 113–117.

Finch, M., Hasalova, P., Weinberg, R.F., and Fanning, C.M., 2014, Switch from thrusting to normal shearing in the Zanskar shear zone, NW Himalaya: Implications for channel flow: Geological Society of America Bulletin, doi: 10.1130/B30817.1.

Frank, W., Hoinkes, G., Miller, C., Purtscheller, F., Richter, W., and Thöni, M., 1973, Relations between metamorphism and orogeny in a typical section of the Indian Himalayas: Tschermaks mineralogische und petrographische Mitteilungen, v. 20, p. 303–332.

Fuhrman, M.L. and Lindsley, D.H., 1988, Ternary-feldspar modeling and thermometry: American Mineralogist, v. 73, p. 201–215.

Ganguly, J., Saxena, S.K., 1984, Mixing properties of aluminosilicate garnets: constraints from natural and experimental data, and applications to geothermo-barometry: American Mineralogist, v. 69, p. 88–97.

Ganguly J, Dasgupta S, Cheng W, Neogi S., 2000, Exhumation history of a section of the Sikkim Himalayas, India: records in the metamorphic mineral equilibria and compositional zoning of garnet: Earth Planet, v. 183, p. 86-471.

Godin, L., Grujic, D., Law, R.D., and Searle, M.P., 2006, Channel flow, ductile extrusion and exhumation in continental collision zones: an introduction: Geological Society, London, Special Publications, v. 268, p. 1–23, doi: 10.1144/GSL.SP.2006.268.01.01.

Grasemann, B., Fritz, H., and Vannay, J.C., 1999, Quantitative kinematic flow analysis from the Main Central Thrust Zone (NW-Himalaya, India): implications for a decelerating strain path and the extrusion of orogenic wedges: Journal of Structural Geology, v. 21, p. 837–853.

Groppo C, Rolfo F, Indares A., 2012, Partial melting in the Higher Himalayan Crystallines of eastern Nepal: the effect of decompression and implications for the "channel flow" model. J. Petrol, v. 53, p. 88-1057.

Grujic, D., Casey, M., Davidson, C., Hollister, L.S., Kündig, R., Pavlis, T., and Schmid, S., 1996, Ductile extrusion of the Higher Himalayan Crystalline in Bhutan: evidence from quartz microfabrics: Tectonophysics, v. 260, p. 21–43, doi: 10.1016/0040-1951(96)00074-1.

Grujic, D., Hollister, L.S., and Parrish, R.R., 2002, Himalayan metamorphic sequence as an orogenic channel: insight from Bhutan: Earth and Planetary Science Letters, v. 198, p. 177–191, doi: 10.1016/S0012-821X(02)00482-X.

Harris N., Inger S., Massey J., 1993, The role of fluids in the formation of the High Himalayan leucogranites, in P. J. T. a. M. P. Searle, ed., Himalayan Tectonics: Geologic Society, London, p. 391-400.

Harris N., Massey J., 1994, Decompression and anatexis of himalayan metapelites: Tectonics, v. 13, no. 6, p. 1537-1546.

Harris, N., Ayres, M., and Massey, J., 1995, Geochemistry of granitic melts produced during the incongruent melting of muscovite: Implications for the extraction of Himalayan leucogranite magmas: Journal of Geophysical Research, v. 100, p. 15767, doi: 10.1029/94JB02623.

Henry, D.J., 2005, The Ti-saturation surface for low-to-medium pressure metapelitic biotites: Implications for geothermometry and Ti-substitution mechanisms: American Mineralogist, v. 90, p. 316–328, doi: 10.2138/am.2005.1498.

Henry, P., Le Pichon, X., and Goffé, B., 1997, Kinematic, thermal and petrological model of the

Himalayas: constraints related to metamorphism within the underthrust indian crust and topographic elevation: Tectonophysics, v. 273, p. 31–56, doi: 10.1016/S0040-1951(96)00287-9.

Herren, E., 1987, Zanskar shear zone: Northeast-southwest extension within the Higher Himalayas (Ladakh, India): Geology, v. 15, p. 409, doi: 10.1130/0091-7613(1987)15<409:ZSZNEW>2.0.CO;2.

Hodges, K.V., and Spear, F.S., 1982, Geothermometry, geobarometry and the Al2SiO5 triple point at Mt. Moosilauke, New Hampshire: American Mineralogist, v. 67, p. 1118–1134.

Hodges, K.V., 2000, Tectonics of the Himalaya and southern Tibet from two perspectives: Geological Society of America Bulletin, v. 112, p. 324–350, doi: 10.1130/0016-7606(2000)112<324:TOTHAS>2.0.CO;2.

Holland, T.J.B., and Powell, R., 1998, An internally consistent thermodynamic data set for phases of petrologic interest: Journal of Metamorphic Geology, v. 16, p. 309–343.

Holland, T.J.B., and Powell, R., 2001, Calculation of phase relations involving haplogranitic melts using an internally consistent thermodynamic dataset: Journal of Petrology, v. 42, p. 83-673.

Holland, T.J.B., and Powell, R., 2011, An improved and extended internally consistent thermodynamic dataset for phases of petrological interest, involving a new equation of state for solids: Thermodynamic dataset for phases of Petrological Interest: Journal of Metamorphic Geology, v. 29, p. 333–383, doi: 10.1111/j.1525-1314.2010.00923.x.

Horton, F., and Leech, M.L., 2013, Age and origin of granites in the Karakoram shear zone and Greater Himalaya Sequence, NW India: Lithosphere, v. 5, p. 300–320, doi: 10.1130/L213.1.

Ireland, T.R., Williams, I.S., 2003, Considerations in zircon geochronology by SIMS, edited by Hanchar, J.M., Hoskins, P.W.O.: Mineral Society of America, Washington, D.C., p. 215–241.

Jain, A.K., Manickavasagam, R.M., Singh, S., 1999, Collision tectonics in the NW Himalaya: deformation, metamorphism, emplacement of leucogranite along the Beas-Parbati Valleys, Himachal Pradesh: Gondwana Research Memoir, v. 6, p. 3-37.

Jamieson, R.A., Beaumont, C., 2013, On the origin of orogens: Geological Society of America Bulletin, v. 125, p. 1671–1702.

Jamieson, R.A., Beaumont, C., Medvedev, S., and Nguyen, M.H., 2004, Crustal channel flows: 2. Numerical models with implications for metamorphism in the Himalayan-Tibetan orogen: Channel Flows and Himalayan Metamorphism: Journal of Geophysical Research: Solid Earth, v. 109, doi: 10.1029/2003JB002811.

Jamieson, R.A., Beaumont, C., Nguyen, M.H., and Grujic, D., 2006, Provenance of the Greater Himalayan Sequence and associated rocks: predictions of channel flow models: Geological Society, London, Special Publications, v. 268, p. 165–182, doi: 10.1144/GSL.SP.2006.268.01.07.

Jamieson, R.A., Beaumont, C., Hamilton, J., Fullsack, P., 1996, Tectonic assembly of inverted metamorphic sequences: Geology, v. 24, p. 839 – 842.

Kohn, M.J., 2014, Himalayan Metamorphism and Its Tectonic Implications: Annual Review of Earth and Planetary Sciences, v. 42, p. 381–419, doi: 10.1146/annurev-earth-060313-055005.

Kohn, M.J., 2008, P-T-t data from central Nepal support critical taper and repudiate large-scale

channel flow of the Greater Himalayan Sequence: Geological Society of America Bulletin, v. 120, p. 259–273, doi: 10.1130/B26252.1.

Kohn, M.J., and Spear, F., 2000, Retrograde net transfer reaction insurance for pressure-temperature estimates: Geology, v. 28, p. 1127, doi: 10.1130/0091-7613(2000)28<1127:RNTRIF>2.0.CO;2.

Kumar, S. and Dobhal, D.P., 1997, Climatic effects and bedrock control on rapid fluctuations of Chhota Shigri glacier, northwest Himalaya, India: Journal of Glaciology, v. 43, p. 467-472.

Lee, J. Y., Marti, K., Severinghaus, J.P., Kawamura, K., Yoo, H.-S., Lee, J.B. & Kim, J.S., 2006, A redetermination of the isotopic abundances of atmospheric Ar: Geochimica et Cosmochimica Acta, v. 70, p. 4507-4512, doi: http://dx.doi.org/10.1016/j.gca.2006.06.1563.

Leech, M., Singh, S., Jain, A., Klemperer, S., and Manickavasagam, R., 2005, The onset of India–Asia continental collision: Early, steep subduction required by the timing of UHP metamorphism in the western Himalaya: Earth and Planetary Science Letters, v. 234, p. 83–97, doi: 10.1016/j.epsl.2005.02.038.

Leech, M.L., Coble, M., Singh, S., Guillot, S., Jain, A.K., 2014a, New U-Pb age and trace element composition of young metamorphic zircon rims from the UHP Tso Morari Complex, NW Himalaya distinguishes peak from retrograde metamorphism: GSA Abstracts with Programs, 46, p. 451.

Leech, M.L., Coble, M., Singh, S., Guillot, S., Jain, A.K., 2014b, New U-Pb age and trace element composition of young metamorphic zircon rims from the UHP Tso Morari Complex, NW Himalaya distinguishes peak from retrograde metamorphism: Eos Trans., Am. Geophys. Union, Fall Meeting Supplement, Abstract T13D-01.

Leger, R.M., Webb, A.A.G., Henry, D.J., Craig, J.A., and Dubey, P., 2013, Metamorphic field gradients across the Himachal Himalaya, northwest India: Implications for the emplacement of the Himalayan crystalline core: Himachal Metamorphic Field Gradients: Tectonics, v. 32, p. 540–557, doi: 10.1002/tect.20020.

Ludwig, K.R., 2003, Isoplot/EX, rev. 3.00, a Geochronological Toolkit for Microsoft Excel: Berkeley Geochronology Center Special Publication, v. 4, p. 71.

Ludwig, K.R., 2009, Squid 2, A user manual, Berkeley Geochronology Center Special Publication No. 5.

Ludwig, K.R., 2012, Isoplot (3.75), a geochronological toolkit for Excel, Berkeley Geochronology Center Special Publication No. 5, p. 75.

McDougall, I., and Harrison, T.M., 1999, Geochronology and thermochronology by the 40Ar/39Ar method, 2nd ed.: New York, NY, Oxford University Press.

Najman Y, Appel E, Boudagher-Fadel M, Bown P, Carter A, et al. 2010. Timing of India-Asia collision: geological, biostratigraphic, and palaeomagnetic constraints: J. Geophys. Res., v. 115.

Nelson, K.D., Zhao, W., Brown, L.D., Kuo, J., Che, J., Liu, X., Klemperer, S.L., Makovsky, Y., Meissner, R., Mechie, J., Kind, R., Wenzel, F., Ni, J., Nabelek, J., et al., 1996, Partially Molten Middle Crust Beneath Southern Tibet: Synthesis of Project Indepth Results: Science, v. 274, p. 1684–1688, doi: 10.1126/science.274.5293.1684.

J.A. Pearce, N.B.W. Harris, A.G. Tindle, 1984, Trace element discrimination diagrams for the tectonic interpretation of granitic rocks: Journal of Petrology, v. 25, p. 956–983.

Peto, P., 1976, An experimental investigation of the melting reactions involving muscovite and paragonite in the silica-saturated portion of the System K2O-Na-2O-Al2O3-SiO2-H2O to 15 kb total pressure:Progress in Experimental Petrology, v. 3, p. 41-45.

Powell, C.M., and Conaghan, P.J., 1973, Plate tectonics and the Himalayas: Earth and Planetary Science Letters, v. 20, p. 1–12, doi: 10.1016/0012-821X(73)90134-9.

Price, R.A., 1986, The southeastern Canadian Cordillera: Thrust faulting, tectonic wedging, and delamination of the lithosphere: Journal of Structural Geology, v. 8, p. 239–254.

Renne, P.R., Swisher, C.C., Deino, A.L., Karner, D.B., Owens, T.L., Depaolo, D.J., 1998, Intercalibration of standards, absolute ages and uncertainties in 40Ar/39Ar dating: Chemical Geology, v. 145, p. 117–152.

Rawat, B.S. and Purohit, K.K., 1988, Geology of the area around Chhota Shigri glacier, Lahul and Spiti district, Technical report on Multi Disciplinary glacier expedition to Chhoat Shigri: Department of Science and Technology, v. 2, p. 157-152.

Robyr, M., Hacker, B.R., and Mattinson, J.M., 2006, Doming in compressional orogenic settings: New geochronological constraints from the NW Himalaya: Doming in the NW Himalaya: Tectonics, v. 25, doi: 10.1029/2004TC001774.

Rubatto D., Chakraborty S., Dasgupta S., 2013, Timescales of crustal melting in the Higher Himalayan Crystallines (Sikkim, Eastern Himalaya) inferred from trace element–constrained monazite and zircon chronology: Contrib. Mineral. Petrol, v. 165, p. 72–349.

Sawyer, E.W., 2001, Melt segregation in the continental crust: distribution and movement of melt in anatectic rocks: Journal of Metamorphic Geology, v. 19, p. 291–309, doi: 10.1046/j.0263-4929.2000.00312.x.

Searle, M.P., 1999, Extensional and compressional faults in the Everest–Lhotse massif, Khumbu Himalaya, Nepal: Journal of the Geological Society, London, v. 156, p. 227 – 240.

Scaillet B., Pecher A., Rochette P., Champenois M., 1995, The gangotri granite (Garhwal Himalaya): laccolithic emplacement in an extending collisional belt: J Geophys Res-Solid Earth, v. 100, no. B1, p. 585-607.

Schlup, M., Steck, A., Carter, A., Cosca, M., Epard, J.-L., and Hunziker, J., 2011, Exhumation history of the NW Indian Himalaya revealed by fission track and 40Ar/39Ar ages: Journal of Asian Earth Sciences, v. 40, p. 334–350, doi: 10.1016/j.jseaes.2010.06.008.

Sharma, P., Ramanathan, A.L., and Pottakkal, J., 2013, Study of solute sources and evolution of hydrogeochemical processes of the Chhota Shigri Glacier meltwaters, Himachal Himalaya, India: Hydrological Sciences Journal, v. 58, p. 1128–1143, doi: 10.1080/02626667.2013.802092.

Singh, K., 2012, Opposite vergent synclines on the flanks of a large-scale box fold in the Chamba–Lahaul region, northwest Himalaya, India: International Journal of Earth Sciences, v. 101, p. 997–1008, doi: 10.1007/s00531-011-0707-6.

Spear FS, Kohn MJ, Cheney JT. 1999. P-T paths from anatectic pelites: Contrib. Mineral. Petrol, v. 134, p. 17–32.

Spear, F. S., 2003, Metamorphic phase equilibria and pressure-temperature-time paths: Mineralogical Society of America, Washington D. C.

Stacey, J.S., and Kramers, J.D., 1975, Approximation of terrestrial lead isotope evolution by a two-stage model: Earth and Planetary Science Letters, v. 26, p. 207–221, doi: 10.1016/0012-821X(75)90088-6.

Steck, A., Spring, L., Vannay, J.C., Masson, H., Stutz, E., Bucher, H., Marchant, R., and Tieche,

J.C., 1993, Geological Transect Across the Northwestern Himalaya in Eastern Ladakh and Lahul–A Model for the Continental Collision of India and Asia: https://www.pim.uzh.ch/_files/_downloads/transect_bucher_1993.pdf (accessed November 2014).

Steiger, R.H., and Jäger, E. 1977, Subcommission on geochronology: Convention on the use of decay constants in geo- and cosmochronology: Earth and Planetary Science Letters, v. 36, p. 359–362, doi: http://dx.doi.org/10.1016/0012-821X(77)90060-7.

Storm, L.C., and Spear, F.S., 2009, Application of the titanium-in-quartz thermometer to pelitic migmatites from the Adirondack Highlands, New York: Journal of Metamorphic Geology, v. 27, p. 479–494, doi: 10.1111/j.1525-1314.2009.00829.x.

Stübner, K., Grujic, D., Parrish, R.R., Roberts, N.M.W., Kronz, A., Wooden, J., and Ahmad, T., 2014, Monazite geochronology unravels the timing of crustal thickening in NW Himalaya: Lithos, v. 210-211, p. 111–128, doi: 10.1016/j.lithos.2014.09.024.

Tajcmanova, L., Connolly, J.A.D., and Cesare, B., 2009, A thermodynamic model for titanium and ferric iron solution in biotite: Journal of Metamorphic Geology, v. 27, p. 153–165.

Thakur, V.C., 1998, Structure of the Chamba nappe and position of the Main Central Thrust in Kashmir Himalaya: Journal of Asian Earth Sciences, v. 16, p. 269–282, doi: 10.1016/S0743-9547(98)00011-7.

Thiede, R.C., Arrowsmith, J.R., Bookhagen, B., McWilliams, M., Sobel, E., Strecker, M., 2006, Dome formation and extension in the Tethyan Himalaya, Leo Pargil, northwest India: Geologic Society of America Bulletin, v. 118, p. 625-650.

Thöni, M., 1977, Geology, structural evolution and metamorphic zoning in the Kulu valley (Himachal Himalayas, India) with special reference to the reversed metamorphism: Mitteilungen der Gesellschaft der Geologie- und Bergbaustudenten in Österreich 24.

Thomas, J.B., Bruce Watson, E., Spear, F.S., Shemella, P.T., Nayak, S.K., and Lanzirotti, A., 2010, TitaniQ under pressure: the effect of pressure and temperature on the solubility of Ti in quartz: Contributions to Mineralogy and Petrology, v. 160, p. 743–759, doi: 10.1007/s00410-010-0505-3.

Unsworth, M.J., Jones, A.G., Wei, W., Marquis, G., Gokarn, S.G., Spratt, J.E., Bedrosian, P., Booker, J., Leshou, C., Clarke, G., Shenghui, L., Chanhong, L., Ming, D., Sheng, J., et al., 2005, Crustal rheology of the Himalaya and Southern Tibet inferred from magnetotelluric data: Nature, v. 438, p. 78–81, doi: 10.1038/nature04154.

Vannay, J.-C., and Steck, A., 1995, Tectonic evolution of the High Himalaya in Upper Lahul (NW Himalaya, India): Tectonics, v. 14, p. 253–263, doi: 10.1029/94TC02455.

Walker, J.D., Martin, M.W., Bowring, S.A., Searle, M.P., Waters, D.J., and Hodges, K.V., 1999, Metamorphism, Melting, and Extension: Age Constraints from the High Himalayan Slab of Southeast Zanskar and Northwest Lahaul: The Journal of Geology, v. 107, p. 473–495, doi: 10.1086/314360.

Webb, A.A.G., 2013, Preliminary balanced palinspastic reconstruction of Cenozoic deformation across the Himachal Himalaya (northwestern India): Geosphere, v. 9, p. 572–587.

Webb, A.A.G., Yin, A., Harrison, T.M., Célérier, J., and Burgess, W.P., 2007, The leading edge of the Greater Himalayan Crystalline complex revealed in the NW Indian Himalaya: Implications for the evolution of the Himalayan orogen: Geology, v. 35, p. 955, doi: 10.1130/G23931A.1.

Webb, A.A.G., Yin, A., Harrison, T.M., Célérier, J., Gehrels, G.E., Manning, C.E., and Grove,

M., 2011, Cenozoic tectonic history of the Himachal Himalaya (northwestern India) and its constraints on the formation mechanism of the Himalayan orogen: Geosphere, v. 7, p. 1013–1061.

White, R.W., Powell, R., Holland, T. J. B., and Worley, B. A., 2000, The effect of TiO2 and Fe2O3 on metapelitic assemblages at greenschist and amphibolite facies conditions: mineral equilibria calculations in the system K2O-FeO-MgO-Al2O3-SiO2-H2O-TiO2-Fe2O3: Journal of Metamorphic Geology, v. 18, p. 497–511.

White, R.W., Powell, R., Holland, T. J. B., 2001, Calculation of partial melting equilibria in the system Na2O-CaO-K2O-FeO-MgO-Al2O3-SiO2-H2O (NCKFMASH): Journal of Metamorphic Geology, v. 19, p. 53-139.

White, R.W., Powell, R., and Holland, T.J.B., 2007, Progress relating to calculation of partial melting equilibria for metapelites: Journal of Metamorphic Geology, v. 25, p. 511–527, doi: 10.1111/j.1525-1314.2007.00711.x.

White, R.W., Powell, R., and Johnson, T.E., 2014, The effect of Mn on mineral stability in metapelites revisited: new a - x relations for manganese-bearing minerals: Journal of Metamorphic Geology, v. 32, p. 809–828, doi: 10.1111/jmg.12095.

Whitney, D.L., and Evans, B.W., 2010, Abbreviations for names of rock-forming minerals: American Mineralogist, v. 95, p. 185–187, doi:10.2138/am.2010.3371.

Williams, M.L. and Grambling, J.A., 1990, Manganese, ferric iron, and the equilibrium between garnet and biotite: Amer. Mineral., v. 75, p. 886-908.

Williams, I.S., 1997, U-Th-Pb geochronology by ion microprobe: not just ages but histories: Society of Economic Geologists Review, v. 7, p. 1–35.

Wyss, M., Hermann, J., and Steck, A., 1999, Structural and metamorphic evolution of the northern Himachal Himalaya, NW India-(Spiti-eastern Lahul-Parvati valley traverse): Eclogae Geologicae Helvetiae, v. 92, p. 3–44.

Yin, A., 2006, Cenozoic tectonic evolution of the Himalayan orogen as constrained by along-strike variation of structural geometry, exhumation history, and foreland sedimentation: Earth-Science Reviews, v. 76, p. 1–131, doi: 10.1016/j.earscirev.2005.05.004.

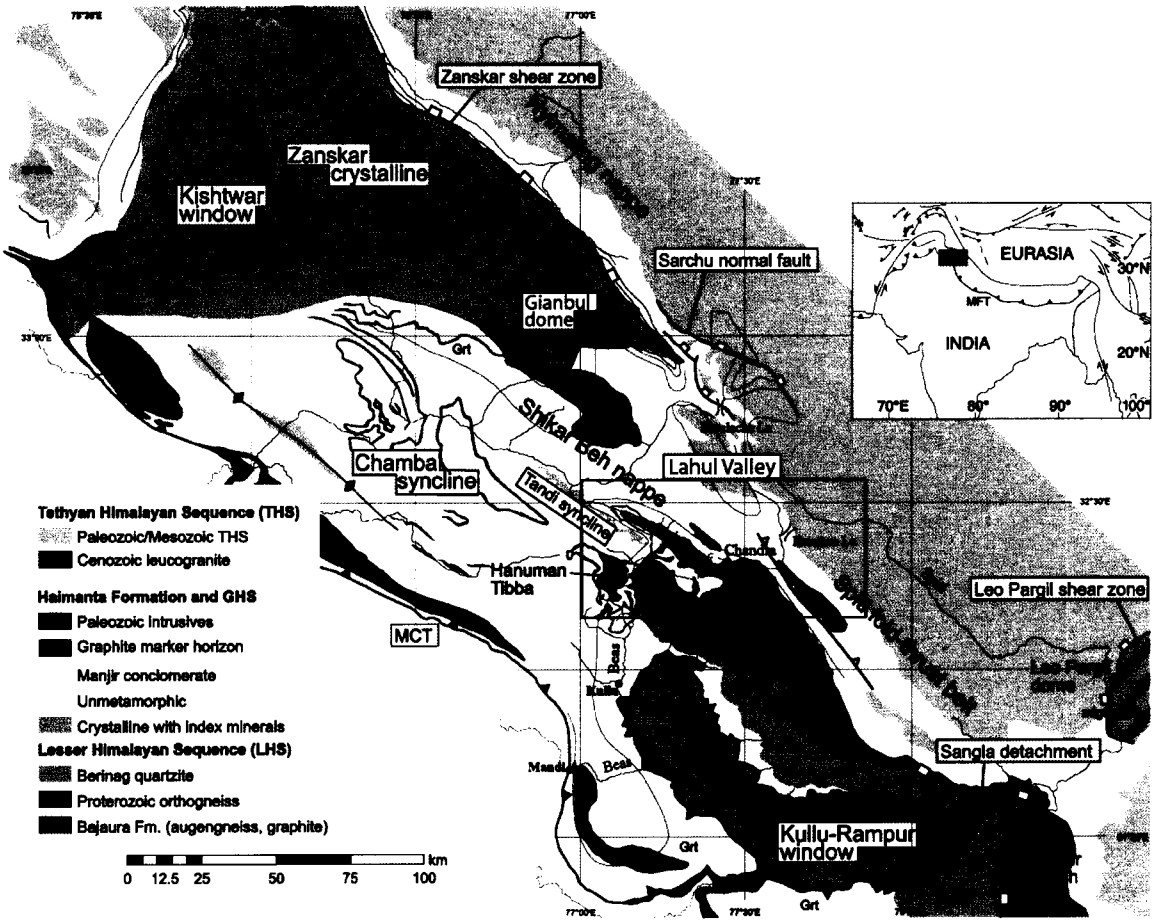

Figure 1: Regional geologic map of the NW Indian Himalaya modified from Stübner et al. (2014).

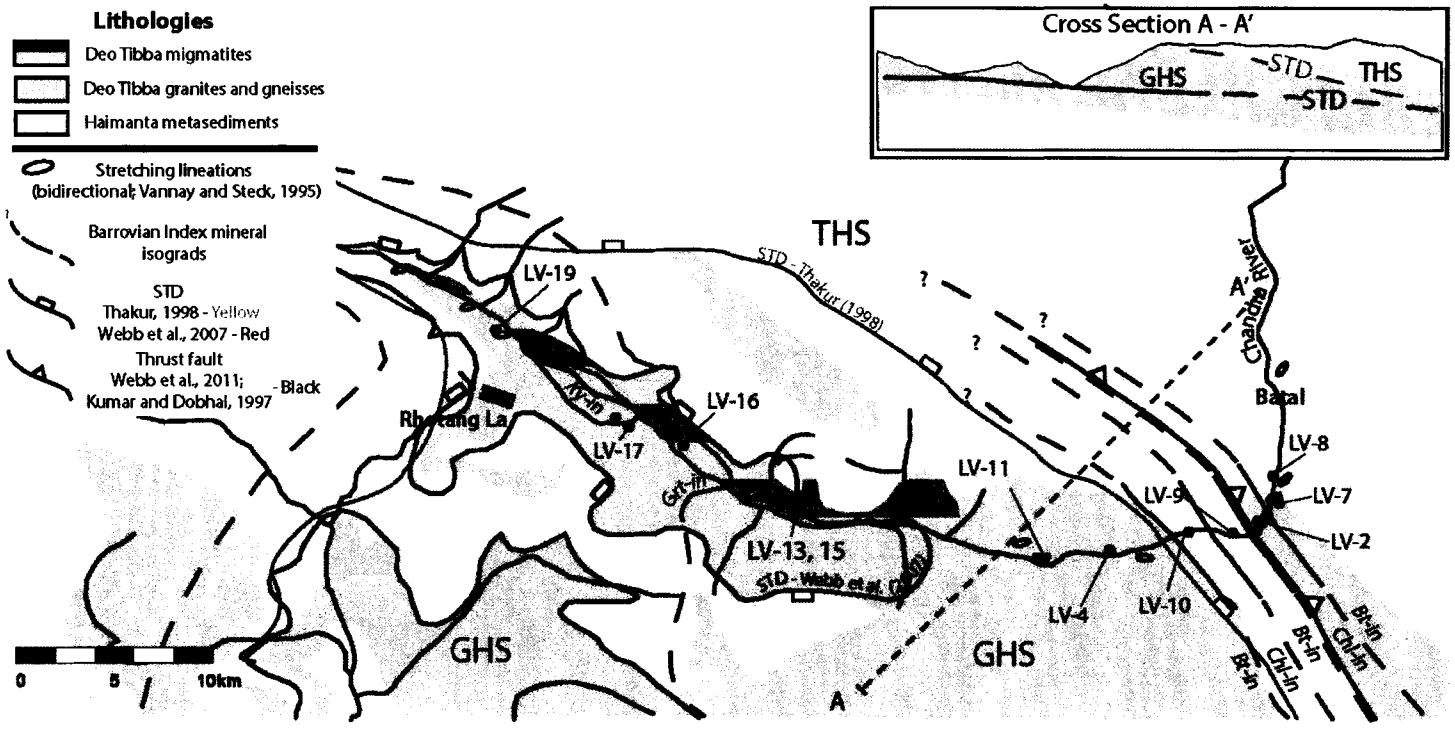

Figure 2: Structural and geologic map of the Lahul valley (LV) including sample locations, isograds, and stretching lineations. Isograds are based on our own observations and those by Dezes (1999) and Stübner et al. (2014). Stretching lineations are compiled by work from this study and by Powell and Conaghan (1973), Frank et al. (1973; 1977), Thoni (1977), Steck et al. (1993), Vannay and Steck (1995), and Wyss (2000). The South Tibetan Detachment (STD) has been mapped by Thakur (1998)—in yellow, and Webb et al. (2007; 2011)—in red. As suggested by Stübner et al. (2014), motion on the STD through the Lahul valley may be diffuse, so all of these branches may have taken up limited amounts of slip. Figure modified from Stübner et al. (2014).

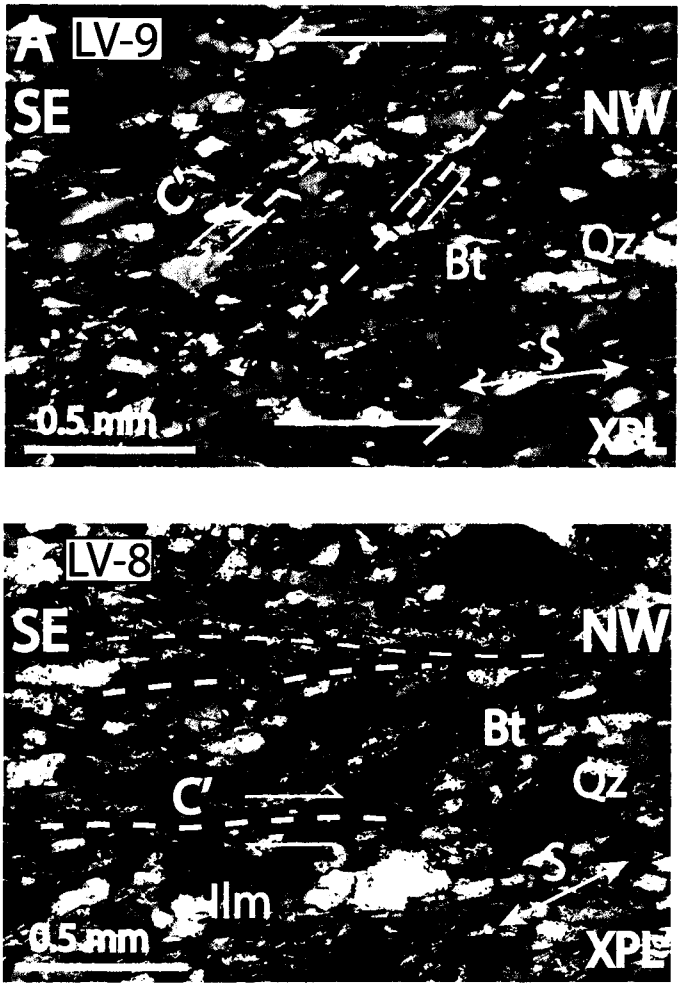

Figure 3: THS samples contain a dominant mineralogy of Qz + Kfs + Pl + Ms ± Bt ± Chl. THS samples have better developed S-C and C'-type shear band cleavage than their GHS counterparts (Fig. 4), and are the best examples of the D3 fabric. These samples contain no evidence of the D2 micro-shear banding used to correlate GHS gneisses to the migmatites. a) Well developed S-C shear fabric defined by Bt3 deformation and quartz recrystallization. b) less-well-developed shear cleavage than LV-9, with undulous extinction in large monocrystalline quartz grains indicating a degree of crystalplastic deformation.

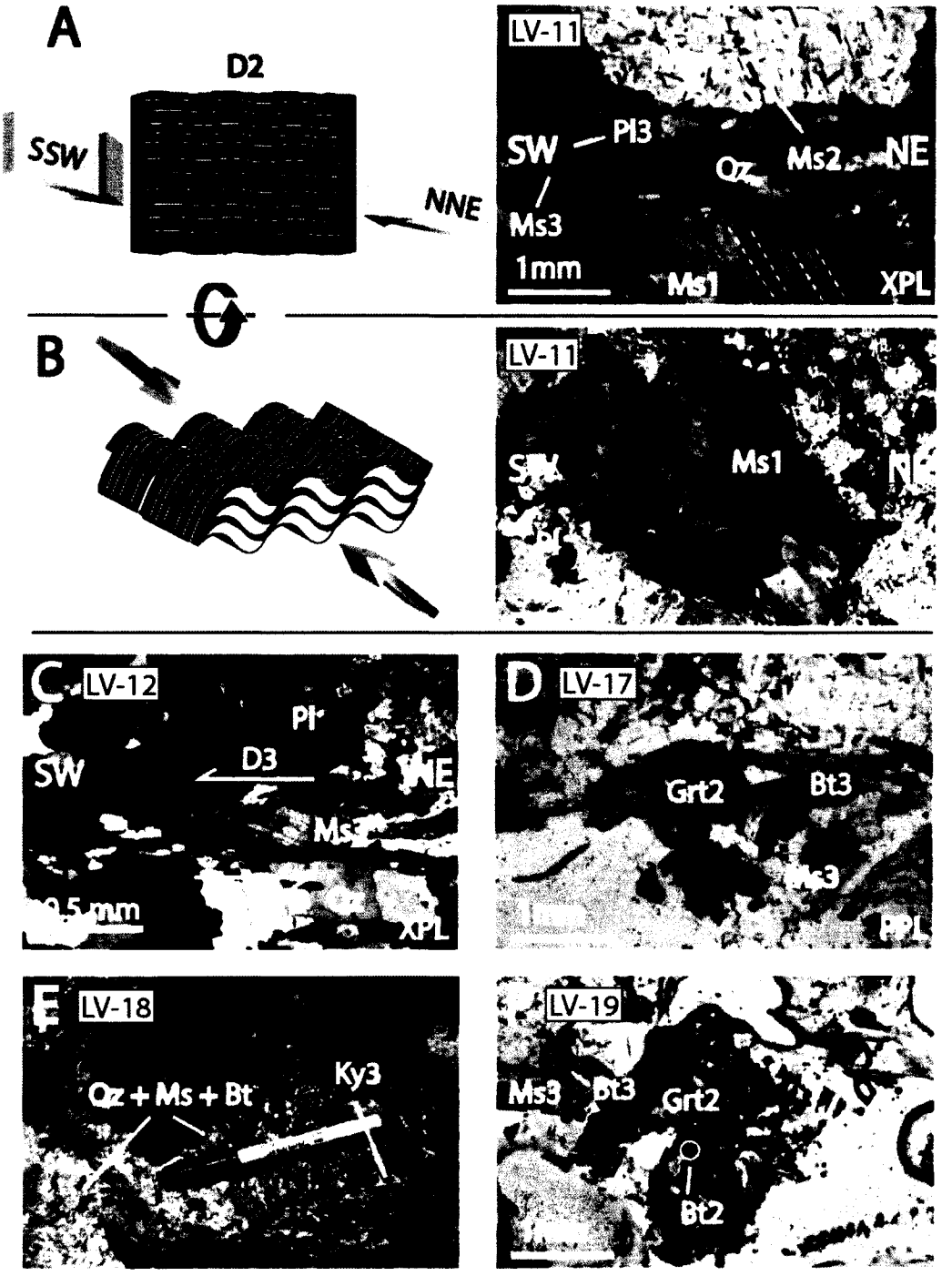

Figure 4: GHS samples contain a dominant mineralogy of Qz + Fsp + Bt + Ms ± Grt ± Ky a) Mantled porphyroclast of Ms1 with D2 crenulation cleavage and post D2 growth of Pl2 with Ms2 inclusions. Illustrated micro-shear-banded Ms1 shows stress orientation

during D2 deformation. b) Illustrated micro-shear-banded Ms1 rotated 90° to better interpret the 3-dimensional stress orientation. c) Top-to-the-SW shear in Ms3 define the dominant D3 foliation plane. d) M2 inclusion-poor Grt1 with Bt3 pairs used for garnet-biotite exchange thermometry. e) Kyanite in biotite-rich quartz vein running through Deo Tibba gneisses; indicative of STD footwall (Webb et al., 2007). f) M2 inclusion-rich garnet with M2 biotite inclusion and Bt3 pairs used for garnet-biotite exchange thermometry.

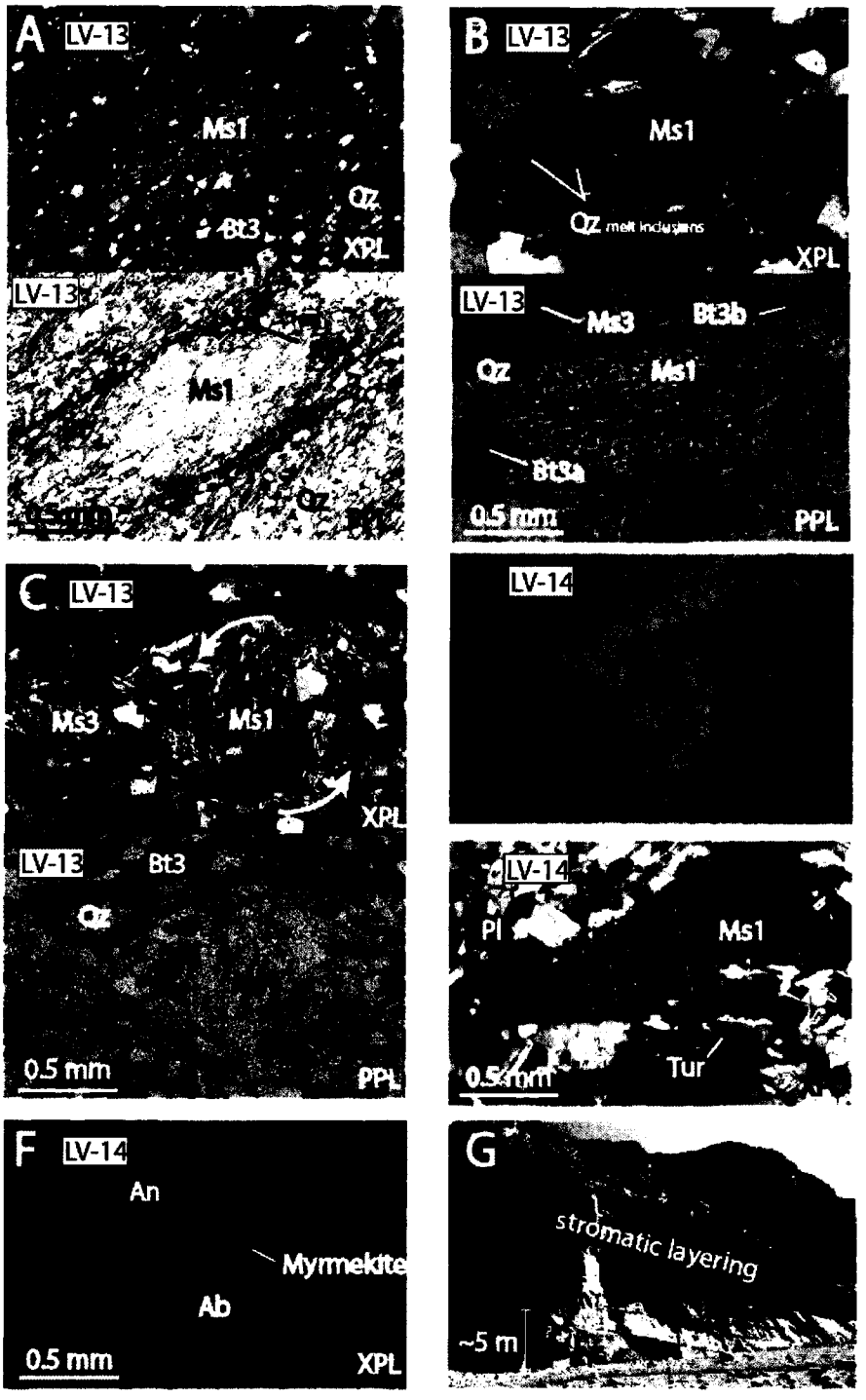

Figure 5: Melanosome LV-13 (a-c) is located near the center of the valley, just past the biotite zone gneisses, containing the assemblage Bt + Qz +Ms + Fsp + Tur + Rt.

Leucosome LV-14 was sampled from a neighboring leucosome next to LV-13, containing the assemblage Ab + An +Ms + Tur + Rt + Qz + rare Bt. a) Rt-filled transgranular microfractures running along the foliation plane above and below mantle porphyroclast of corroding Ms1. b) Corrosion of mantle Ms1 porphyroclast produced melt pockets of Qz. Bt3a replacement of Ms1 indicates continuing metamorphism near peak conditions outside of muscovite stability fields. Bt3 and Ms3 interfingering in the matrix indicates the dominant foliation was produced during retrograde conditions within the muscovite stability fields, indicating the dominant D3 fabric is retrograde c) Rotated mantle porphyroclast of dehydrating Ms1 indicating some transport during melt segregation. d) Melt pool of Fsp in degrading prograde Tur. e) Preserved mantled porphyroclast of micro-shear-banded Ms1, indicating migmatization occurred in the Deo Tibba gneisses instead of THS metapelites; which do not contain micro-shear-banded Ms1. f) Intergrowth of Ab and An, with retrograde myrmekite.

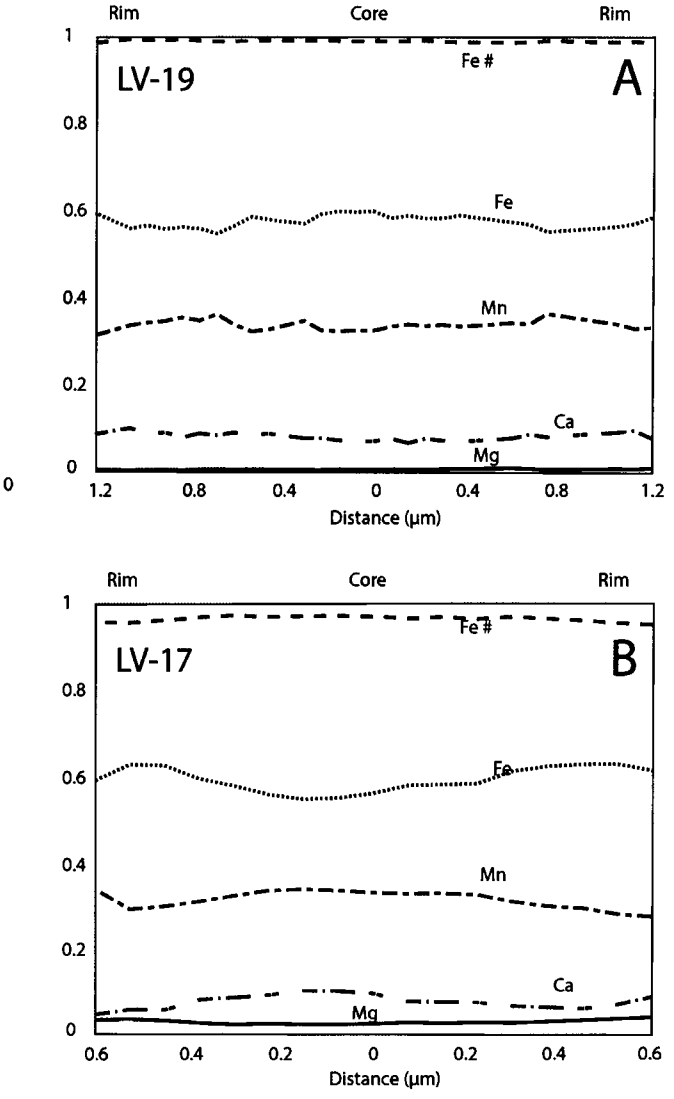

Figure 6. Garnet zoning profiles normalized to major cations Ca, Fe, Mn, Mg: a) LV-19 showing overall prograde metamorphic growth, with zoning patterns showing a slight decrease in temperature from the core to inner rim, and slight increase in temperature from the inner rim to outer rim, with a relatively flat, low Ca content profile indicating baric conditions b) LV-17 Typical prograde zoning seen by decrease in Mn with increasing Fe toward the garnet rim.

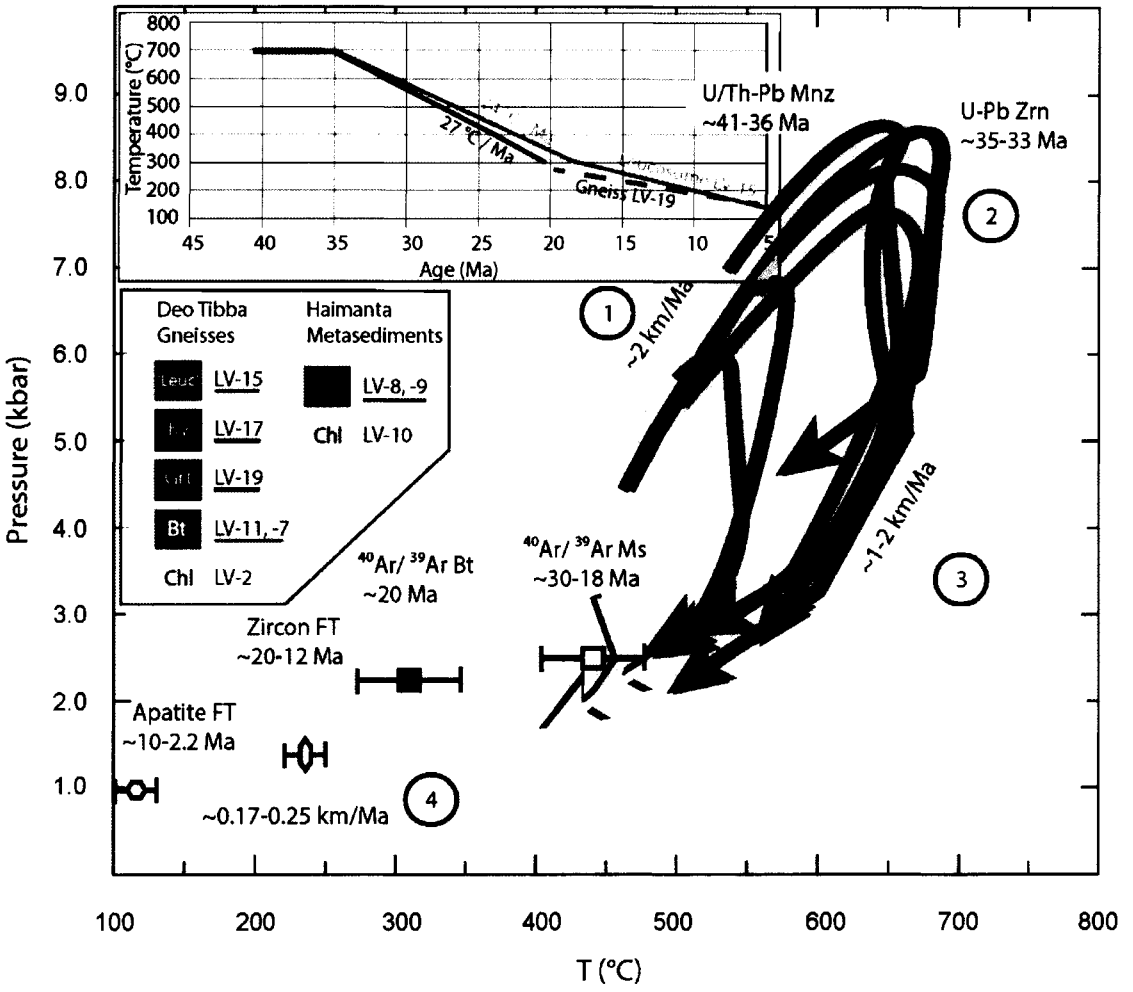

Figure 7: P-T paths for Deo Tibba gneisses, migmatites, and Haimanta metasediments in Lahul valley, modeled in the system Na_2O-CaO-K_2O-FeO-MgO-MnO-Al_2O_3-SiO_2-TiO_2. Circled numbers correspond to different stages along P-T paths (see text).

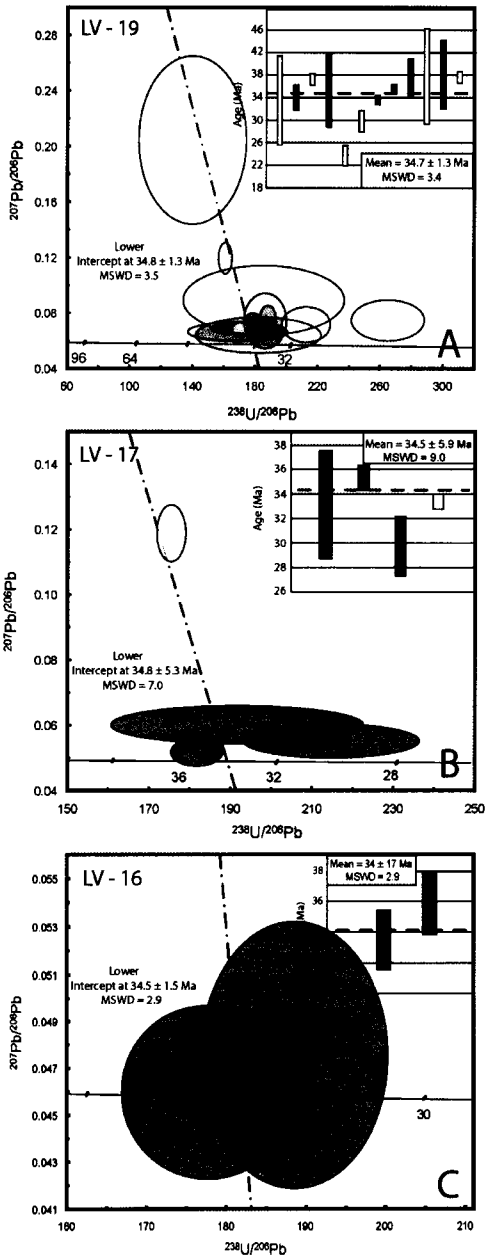

Figure 8: Tera-Wasserberg concordia diagrams showing U-Pb SHRIMP analyses for metamorphic and magmatic zircons from samples LV-19, -17, and -16. Mean ages are calculated from ^{207}Pb-corrected $^{206}Pb/^{238}U$ ages, with box heights showing 2σ errors. Intercept ages are fixed to $^{207}Pb/^{206}Pb$=0.837, with error ellipses showing 2σ error. Yellow ellipses and boxes were omitted, based on selection criteria.

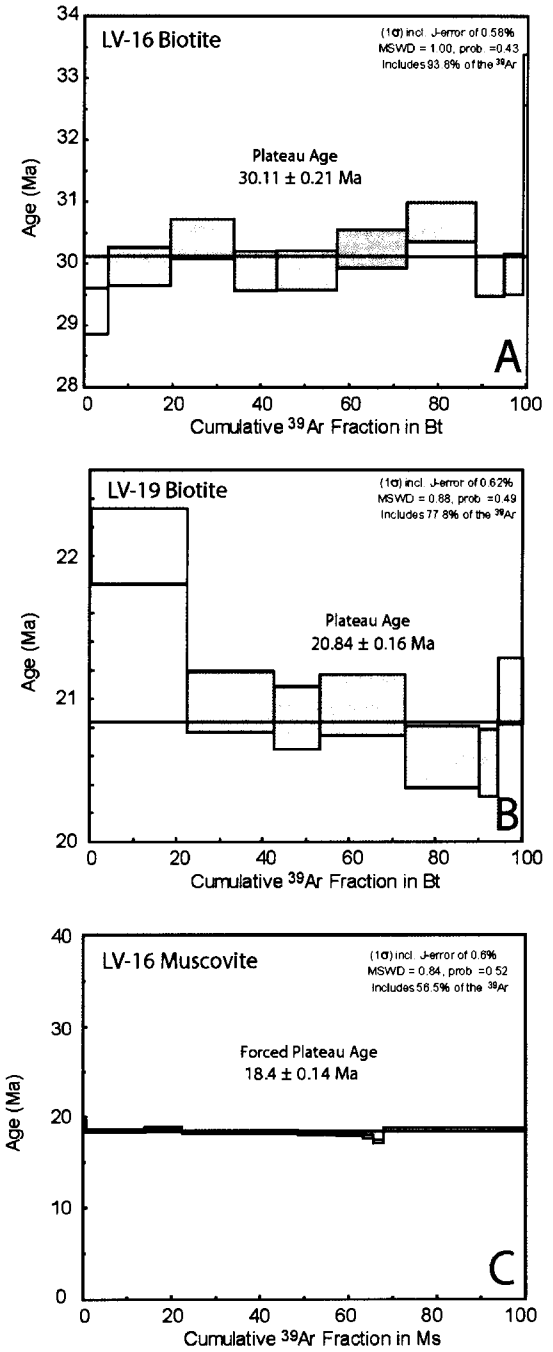

Figure 9: $^{40}Ar/^{39}Ar$ in biotite and muscovite plateau ages for representative samples LV-16 (a, c) and LV-19 (b). Plateau steps are in magenta, rejected steps are in yellow.

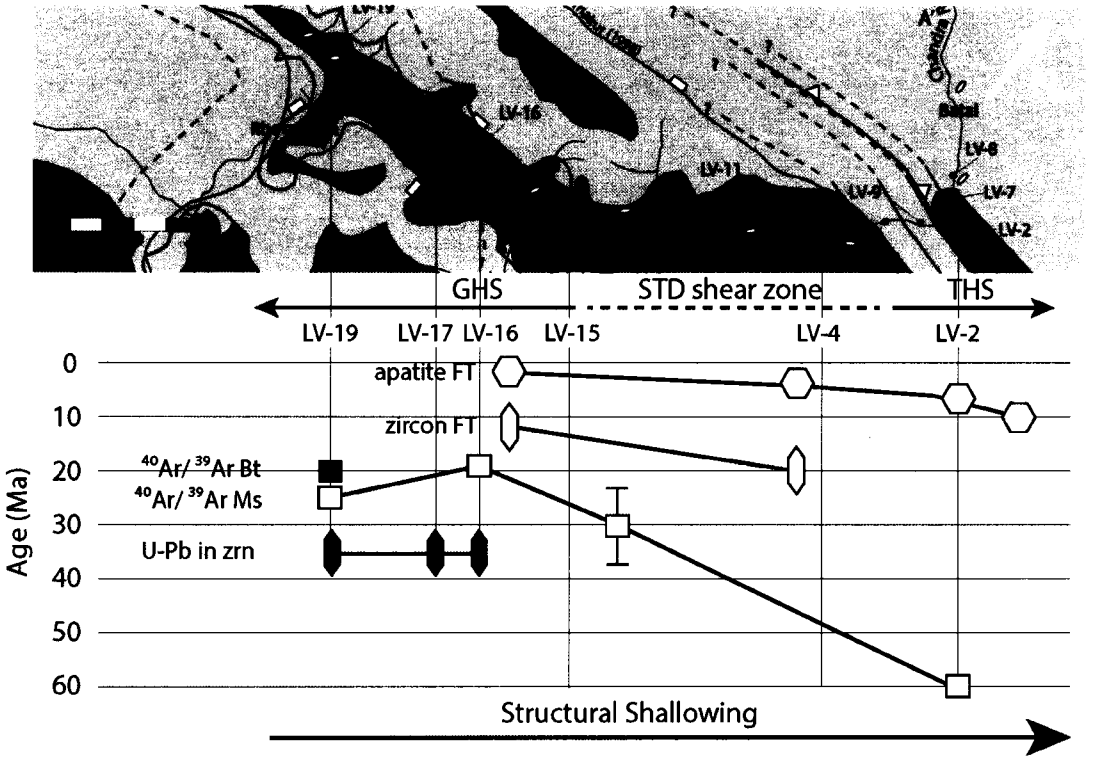

Figure 10: Correlation of cooling histories for Deo Tibba gneisses and Haimanta metasediments in a transect perpendicular to the STD through Lahul, incorporating zircon and apatite fission track dates from Schlup et al. (2011), $^{40}Ar/^{39}Ar$ muscovite dates from Stübner et al. (2014), and U-Pb in zircon and $^{40}Ar/^{39}Ar$ muscovite and biotite ages from this study.

Table 1: Major element data from whole rock XRF, and rare earth element (REE) and trace element data from inductively-coupled plasma-mass spectrometry (ICP-MS) from representative samples used in thermodynamic modeling and rock classification.

Whole Rock XRF

Unnormalized Major Elements (Weight %)

	Haimantas			Deo Tibba						
	LV-8	LV-9	LV-10	LV-2	LV-7	LV-11	LV-13	LV-15	LV-17	LV-19
SiO_2	72.54	68.97	61.53	74.06	71.90	72.80	56.02	74.71	72.50	76.74
TiO_2	0.54	0.50	0.82	0.22	0.38	0.26	0.78	0.16	0.30	0.06
Al_2O_3	13.17	13.79	17.00	14.51	13.94	14.57	19.28	14.00	14.11	13.19
FeO*	3.33	4.96	5.06	1.43	2.45	1.83	7.99	1.35	2.39	0.61
MnO	0.04	0.07	0.07	0.06	0.02	0.02	0.09	0.02	0.07	0.03
MgO	2.07	2.65	6.29	0.95	2.43	0.44	4.09	0.33	0.61	0.10
CaO	0.16	2.60	1.02	0.34	0.37	0.83	1.06	0.80	0.83	0.46
Na_2O	0.45	2.92	1.65	2.90	2.50	2.75	2.61	3.11	3.12	3.86
K_2O	3.47	2.32	1.95	3.25	3.98	5.80	5.47	4.29	4.39	4.00
P_2O_5	0.05	0.13	0.16	0.19	0.17	0.18	0.18	0.12	0.17	0.25
Sum	95.81	98.91	95.55	97.90	98.16	99.49	97.56	98.89	98.48	99.29
LOI %	3.95	0.72	3.65	1.43	1.61	0.30	1.22	0.66	0.63	0.46

ICP-MS

REE and Trace Elements (ppm)

	Haimantas			Deo Tibba						
La	23	31	41	24	25	31	53	17	24	4
Ce	46	60	81	53	54	68	108	36	51	9
Pr	5	7	10	6	7	8	12	4	6	1
Nd	20	25	36	23	24	31	43	16	23	4
Sm	4	5	8	6	6	8	9	4	5	1
Eu	1	1	1	0	1	1	2	0	1	0
Gd	4	5	7	5	6	8	7	3	4	1
Tb	1	1	1	1	1	1	1	1	1	0
Dy	4	5	7	5	5	5	7	3	5	2
Ho	1	1	1	1	1	1	1	1	1	0
Er	2	3	4	2	3	1	4	2	2	1
Tm	0	0	1	0	0	0	1	0	0	0
Yb	2	2	3	2	2	1	3	2	2	1
Lu	0	0	1	0	0	0	1	0	0	0
Ba	792	1711	280	140	210	371	1380	266	295	34
Th	16	10	18	15	17	23	24	13	15	3
Nb	12	10	15	18	15	16	15	9	13	13
Y	22	25	35	24	26	17	34	18	25	8
Hf	5	3	5	3	4	3	4	2	4	1
Ta	1	1	1	7	2	1	1	1	1	3
U	4	2	3	4	5	5	8	3	10	9
Pb	7	31	13	74	4	41	38	33	31	19
Rb	174	115	59	299	274	334	338	269	369	465
Cs	9	13	2	36	49	17	34	13	36	44
Sr	32	181	65	21	31	67	124	44	66	13
Sc	12	11	18	6	7	4	22	5	7	4
Zr	167	113	186	94	148	113	134	75	120	27

Table 2: Representative mineral compositions (apfu) for garnet-biotite pairs in LV-19 and LV-17. Fe^{3+} contents for garnet were estimated using the program AX (Holland, 2009) that recalculates garnets to eight cations per 12 oxygens. For Ti-in-biotite thermometry, biotites were calculated to 22 apfu.

Sample #	LV-19		LV-17
Garnet apfu (O=12)			
	Inclusion	**Rim**	
Fe	1.825	1.7935	1.809
Mn	0.954	0.951	0.953
Mg	0.022	0.0185	0.020
Ca	0.141	0.1995	0.170
Xalm	62.0	60.5	61.3
Xsps	32.4	32.1	32.3
Xpyr	0.7	0.6	0.7
Xgrs	4.8	6.7	5.8
Biotite apfu (O=22)			
	Inclusion	**Matrix**	
Si	5.572	5.586	5.579
Ti	0.286	0.305	0.296
Al	3.502	3.519	3.510
Cr	0.002	0.001	0.002
Fe^{2+}	3.190	3.143	3.166
Fe^{3+}	0.435	0.429	0.432
Mn	0.107	0.117	0.112
Mg	0.339	0.281	0.310
Ca	0.001	0.005	0.003
Na	0.033	0.051	0.042
K	1.877	1.872	1.874
	Hodges and Spear, 1982		
5 kbar	**500**	**511**	**523**
8 kbar	**510**	**521**	**533**
	Ferry and Spear, 1978		
5 kbar	**482**	**486**	**499**
8 kbar	**492**	**496**	**509**
	Gangula and Saxena, 1984		
5 kbar	**627**	**634**	**612**
8 kbar	**638**	**645**	**623**
	Williams and Grambling, 1990		
5 kbar	**602**	**614**	**612**
8 kbar	**612**	**624**	**622**
	Ti-in-Bt Thermometry (°C)		
	620	**632**	**623**

Table 3: Sample locations, lithologies, dating techniques, thermometry methods, and Perple_X modeled P-T estimates.

Sample Number	Latitude/ Longitude	Rock Type	Thermochronometry (Ma)			Thermometry (°C)		P-T Estimate from Modeling	
			$^{40}Ar/^{39}Ar$ Bt	$^{40}Ar/^{39}Ar$ Ms	U-Pb in Zrn	Ti-in-Bt	Ti-in-Qz	Temp (°C)	P (kbar)
LV-19	N 32°23'45.6000", E 77°15'12.9600"	Qfp augen gneiss	20.8 ± 0.2		34.8 ± 1.3	630 ± 14*, n=25	636 ± 43, n=7	470 - 670 °C	3.4 - 9.0 kbar
LV-18	N 32°23'45.6000", E 77°15'12.9600"	Qfp augen gneiss							
LV-17	N 32°21'51.3576", E 77°17'53.5200"	Qfp augen gneiss			34.8 ± 5.3	621 ± 11, n=21	630 ± 70, n=20	375 - 680 °C	4.0 - 9.0 kbar
LV-16	N 32°21'32.6196", E 77°18'13.4028"	Migmatite	30.1 ± 0.2	18.4 ± 0.1	34.5 ± 1.5				
LV-15	N 32°20'05.2548", E 77°20'22.4916"	Leucosome-Qfp gneiss						620 - 700 °C	6.5 - 9.0 kbar
LV-14	N 32°19'23.3688", E 77°21'26.0100"	Leucosome-Qfp gneiss			—	653 ± 14*, n=27	616 ± 101, n=4		
LV-13	N 32°18'17.1360", E 77°27'24.4728"	Melanosome-schist				612 ± 6, n=20	692 ± 61, n=23		
LV-11	N 32°17'31.4196", E 77°28'51.6396"	Qfp augen gneiss			—			620 - 660 °C	3.6 - 9.0 kbar
LV-4	N 32°17'49.3728", E 77°31'25.6476"	Leucogranite			—				
LV-10	N 32°18'08.9208", E 77°33'58.3200"	Chlorite schist						450 - 500 °C	<1.0 - 3.5 kbar
LV-9	N 32°18'26.9280", E 77°35'03.5088"	Slate-phyllite						500 - 550 °C	3.6 - 7.0 kbar
LV-2	N 32°18'50.6340", E 77°36'35.1900"	Qfp gneiss			—			< 470 °C	< 3.6 kbar
LV-7	N 32°19'40.1700", E 77°36'41.6088"	Qfp gneiss						< 680 °C	< 9.0 kbar
LV-8	N 32°19'41.6820", E 77°36'41.1948"	Phyllite-schist				667 ± 3, n=4	599 ± 66, n=46	475 - 580 °C	3.4 - 7.0 kbar

Note: Ti-in-biotite and Ti-in-quartz temperatures were calibrated to Henry et al. (2002) and Thomas et al. (2010) respectively. Ti-in-biotite thermometry has an uncertainty of ± 24°C for temperatures >700°C and 12°C for temperatures <700°C. Thermochronometry contains averages of calculated temperatures, with an error based on one standard deviation from the mean, where N=number of spots analyzed. An * indicates that the sample contains XMg <0.275 - under the required amount for the Ti-in-biotite thermometer, increasing the uncertainty of the temperature estimate. Ti-in-quartz was calculated at 6 kbar for LV-19 (prograde Qz inclusions in Grt) and LV-8 (lower P stability predicted by modeling), and at 8 kbar for all other samples. P-T stability is based on the constraints of the peak metamorphic assemblage from pseudosections modeled in Perple_X.

Table 4: Stages of metamorphism and deformation seen in thin section

M1/D1: Identifyed by mantled porphyroclasts of D2 micro-shear-banded Ms1. Since these occur in both Ky grade and Chl grade Deo Tibba gneisses, they may be inherited grains from their granitic protolith **D2:** NNE/SSW to ENE/WSW strain recorded as micro-shear-banding in Ms1 **M2:** Identifyed by post kinematic mantled prophyroclasts of Pl2, with Ms2 inclusions oriented along both the axial traces of microshear bands and the basal cleavage in Ms1 (Figure 3a). Tur, Rt, Grt, and Ky occur as matrix porphyroclasts formed prior to M3/D3, though their relation to M1/D1, D2, and M2 is not clear in petrography. Since these minerals are undeformed, they are categorized as part of the M2 assemblage **M3/D3:** Development of predominant foliation and shear cleavage, seen in Qz, Fsp, Ms, and Bt. Note that M3/D3 developed under different PT stages between samples. Ie: GHS M3/D3 fabric developed between prograde and peak T conditions, while M3/D3 fabric in the migmatites developed as a retrograde assemblage **M4:** Retrograde mineral growth of Ms, Chl, and Rt.

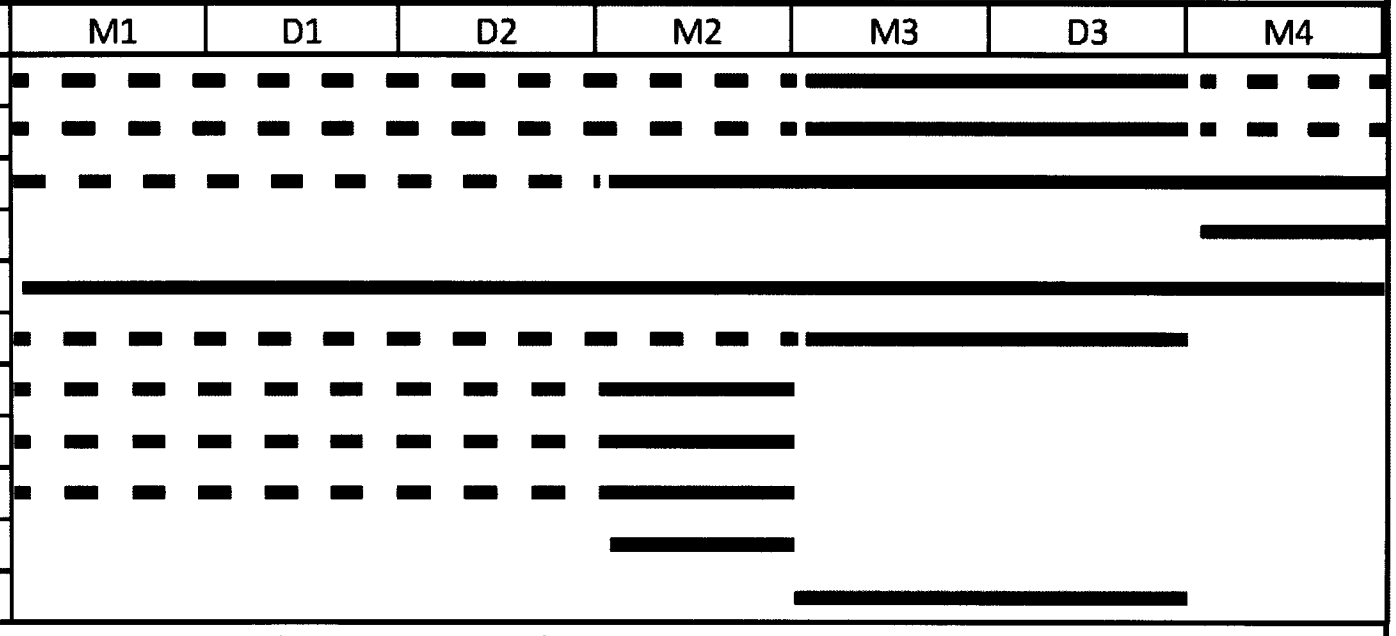

Note: Bold lines represent the stages of metamorphism and deformation seen in thin section; dashed lines indicate the probable mineral assemblage during each stage.

Table 5: Thermal and mechanic model predictions for observations through Lahul Valley

Criterion	Channel flow	Critical taper	Lahul Valley
P at peak T	13 to 7 kbar at 800 °C	12 kbar at 800 °C	8 kbar at 700 °C
Field T gradient	Decreasing T structurally upward	Increasing T structurally upward	N.D.
Field P gradient	Decreasing P structurally upward	N.D.	N.D.
High-T retrograde P-T path	Isothermal exhumation	Isobaric cooling	Isothermal exhumation & Isobaric cooling
Peak age 16,	15–20 Ma	15–20 Ma	35 Ma
Duration at high T	>10–15 m.y.	~5 m.y.	~1 m.y. (could be further constrained Mnz)
Initial cooling age	8–9 Ma	15–20 Ma	N.D.
Cooling rate (to 400°C)	70 °C/m.y.	40–45 °C/m.y.	25-30 °C/m.y.

Note: Channel flow model predictions after Jamieson et al., 2004; Critical taper model predictions after Henry at al., (1997) and Bollinger et al., (2006); N.D. - not determined

Modified from Kohn, 2008

Appendix 1: Table of SHRIMP-RG U-Pb analyses.

Spot Name	Hf (ppm)	U (ppm)	Th (ppm)	$^{232}Th/^{238}U$	$^{204}Pb/^{206}Pb$	^{206}Pb (%)	$^{238}U/^{206}Pb$	$^{207}Pb/^{206}Pb$	$^{206}Pb/^{238U}$ Age	1σ err
LV16-2.1	16046	1973	16	0.008	0.000	0.24	193.66	0.05	33.12	1.05
LV16-4.1	15537	3648	23	0.006	0.000	0.02	179.87	0.05	35.73	1.11
LV17-2.1	10454	1662	23	0.012	0.002	1.42	191.25	0.06	33.14	2.19
LV17-32.1	12739	4667	70	0.013	0.001	0.32	181.32	0.05	35.34	0.51
LV17-8.1	13948	2290	37	0.015	0.001	0.78	214.39	0.05	29.76	1.22
LV17-12.1*	17269	3909	73	0.016	0.005	9.06	175.04	0.12	33.41	0.32
LV19-9.1*	17241	2058	56	0.024	0.002	4.57	183.10	0.08	33.51	3.94
LV19-10.1	24439	2431	69	0.025	0.003	2.62	184.11	0.07	34.01	1.11
LV19-45.1*	27792	3267	174	0.042	0.008	8.55	158.02	0.11	37.20	0.49
LV19-1.1	22291	3160	82	0.024	0.001	1.24	179.72	0.06	35.33	3.28
LV19-6.1*	25142	1314	25	0.017	0.001	2.69	264.01	0.07	23.72	0.89
LV19-49.1*	23189	3992	77	0.018	0.001	2.26	210.73	0.06	29.83	0.93
LV19-7.1	18546	2079	47	0.020	0.002	2.92	185.85	0.07	33.58	0.40
LV19-12.1	20578	1894	48	0.024	0.001	2.74	176.03	0.07	35.52	0.38
LV19-55.1	23273	2293	66	0.027	0.002	1.90	167.46	0.06	37.65	1.63
LV19.10.1T*	20314	1556	51	0.030	0.010	19.76	136.66	0.20	37.74	4.24
LV19T2	22445	2689	64	0.023	0.002	1.56	166.12	0.06	38.09	3.03
LV19-15.1*	19737	3198	62	0.018	0.002	1.77	167.93	0.06	37.60	0.52

Note: Individual analyses which yielded Paleogene ages for the first 2 or more cycles, and the age increased more than ca. 20 Ma over the subsequent cycles of data acquisition, were interpreted to reflect depth profiling into an older age domain with depth. Because the ion-probe pits are generally Gaussian-shaped, the increase in ages reflects mixing between the bottom of the pit and the sides. We reduced the data with only the youngest 3, 5, and 7 cycles to calculate model ages for the zircon surface-rim ages. An * next to the spot name indicates the sample was omitted from sample age calculations based on criteria stated in the methods section.

Appendix 2:

The effect of MnO in the stabilization of garnet at low P-T conditions is well documented in metapelites, requiring special considerations for modeling garnet stability, especially at low P-T (White et al., 2005; White et al., 2014). Thermodynamic modeling in MnO and MnO free systems have shown that the presence or absence of MnO only has ~1% effect on the stability of all mineral phases other than garnet. When modeling with MnO, garnet is seen in low modal abundances <1% in low P-T space, until reaching a threshold near the garnet stability in NKFMASH, at which point the modal abundance of garnet increases to several modal percent. Since our samples contain less than 1% garnet, garnet growth is likely occurring at low to mid P-T conditions, beneath the garnet stability predicted in KFMASH systems. In addition, high Mn content in garnet rims and cores suggest that garnet growth is occurring outside of KFMASH garnet stability, making the incorporation of MnO in our modeling an important factor for garnet stability.

Since chlorite is a Mn bearing mineral, the incorporation of MnO in chlorite is, by extension, important to garnet stability at low P-T. We used calculations of MnO content from the MnO bearing Chl(HP) model as a proxy for the effect of MnO on our non MnO bearing Chl(W) model. We plotted isopleths of modal abundance of chlorite and MnO content, then choosing the highest modal abundance and highest MnO content calculated the largest possible impact on the total bulk rock MnO content caused by MnO incorporation in the Chl(HP) solution model. We mirrored this effect into the hp11 database by tweaking the bulk rock composition to reflect the point of maximum MnO incorporation in chlorite (as calculated in hp04). This gave us an estimate of how MnO in chlorite may be effecting garnet stability within the hp11 database without actually incorporating a MnO chlorite solution model.

Biotite compositions are highly sensitive to the O_2 component. In samples with large quantities of biotite, and a potential significant amount of Fe^{3+}, our modeling doesn't work very well. The Ti concentrations of biotite are significantly lower for a given temperature then in more felsic compositions. Compositional zoning of Ti-in-biotite predicted by our modeling does not align perfectly with our microprobe data. When systematically adding O_2 to the system, biotite compositions matching our microprobe data shift to higher P-T, as predicted by the thermometer. We adjusted O_2 up to 12% FeO to better constrain our modeling toward our microprobe data. While this did help in altering biotite compositions to reflect similar P-T space between our pseudosection modeling and our biotite thermometry, it also destabilized garnet, changed zoisite to epidote, and introduced significant excess O_2, leading us to beiieve we should model in an O_2 free system.

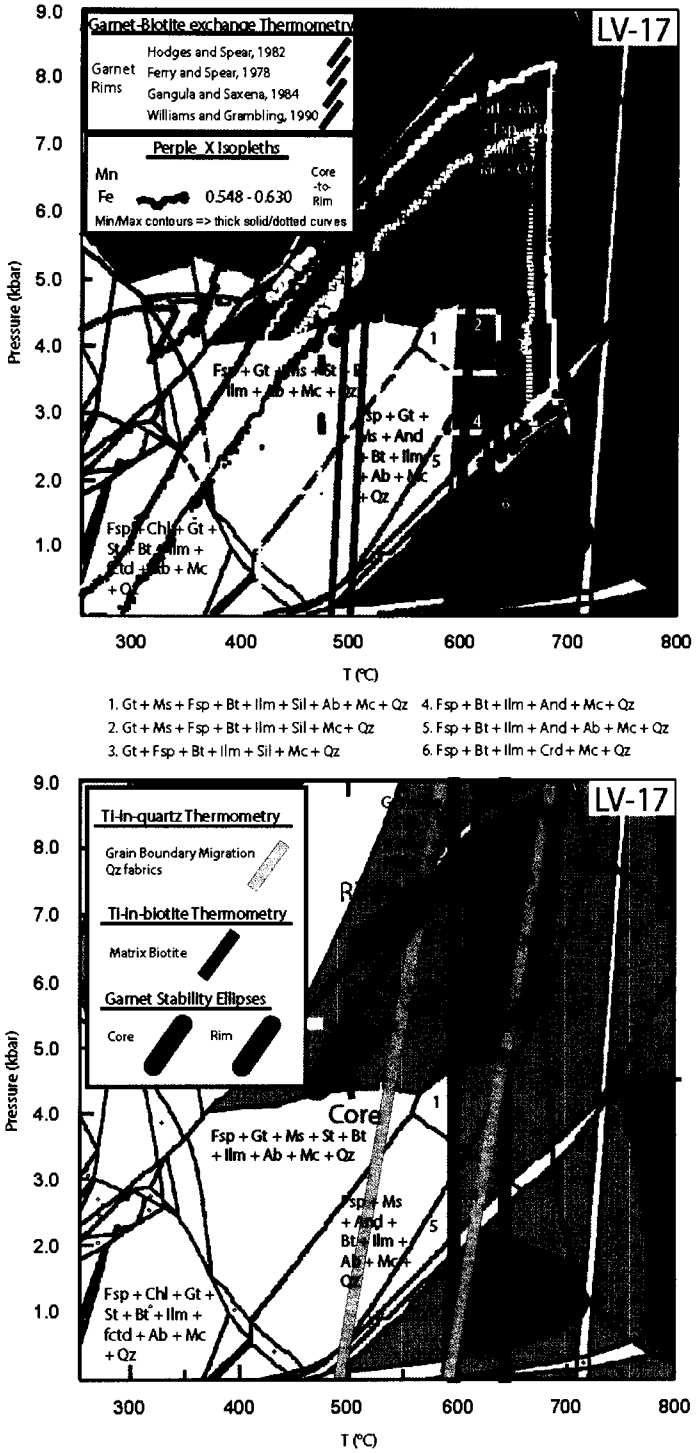

Appendix 3a: Pseudosections for garnet grade Deo Tibba gneiss LV-17 calculated using whole rock chemistry by Perple_X. All phase diagrams are made in the hp11 database in the MnNCKFMASHT system, saturated with SiO2; H20 cannot be a saturated component using melt(W). Garnet stability fields and isopleths are calculated in the hp04 database in an equivalent system. Core, rim and outer rim data are based on microprobe garnet compositions for Fe and Mg, and plotted by Perple_X. Garnet biotite exchange thermobarometry from garnet rims are plotted as lines, with calibrations from Ferry and Spear (1978)-red, Hodges and Spear (1982)-green, Gangula and Saxena (1984)-purple, and Williams and Grambling (1990)-blue. Garnet stability ellipses (in orange shades) are interpretations of where garnet cores and rims are stable based on garnet-biotite thermometry and garnet chemistry predicted by Perple_X. Ti-in-quartz and Ti-in-biotite thermometry are plotted as thick lines constraining the range of temperatures predicted by the thermometer; blue for quartz inclusions in garnet, light green for biotite inclusions in garnet, and dark green for matrix biotite. Thick blue lines with arrows show predicted P-T paths for samples based on mineral field stability, garnet-biotite exchange thermometry, and Ti-in-biotite and Ti-in-quartz thermometry. Mineral abbreviations from Whitney and Evans, 2010.

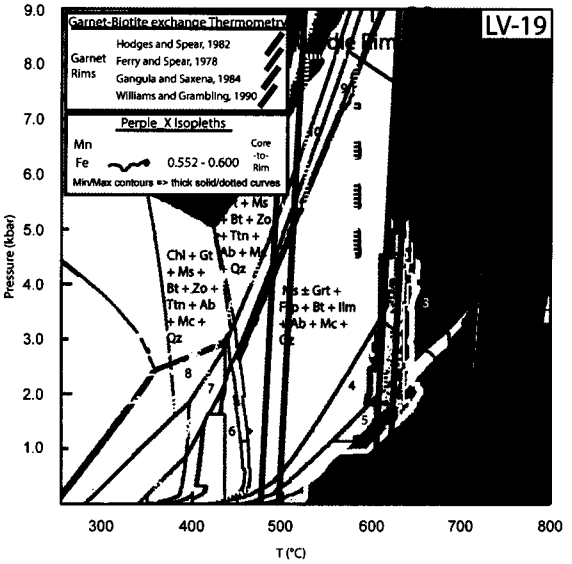

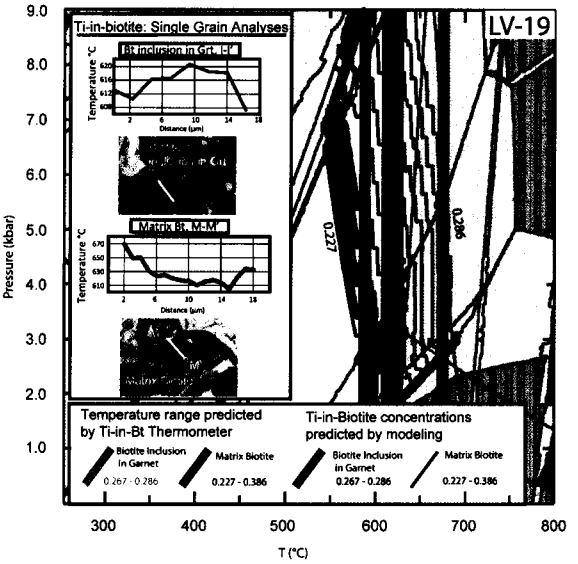

1. Gt + Ms + Fsp + Bt + Ilm + Mc + Qz
2. Gt + Fsp + Bt + Ilm + Sill + Ab + Mc + Qz
3. Gt + Fsp + Bt + Ilm + Sil + Mc + Qz
4. Gt + Fsp + Bt + Ilm + And + Ab + Mc + Qz
5. Gt + Fsp + Bt + Ilm + Crd + And + Ab + Mc + Qz
6. Fsp + Chl + Ms + Ilm + Ab + Mc + Qz
7. Fsp + Chl + Gt + Ms + Ttn + Ab + Mc + Qz
8. Fsp + Chl + Gt + Ms + Zo + Ttn + Ab + Mc + Qz
9. Gt + Ms + Fsp + Bt + Ab + Mc + Rt + Qz
10. Gt + Ms + Fsp + Bt + Ttn + Ab + Mc + Qz

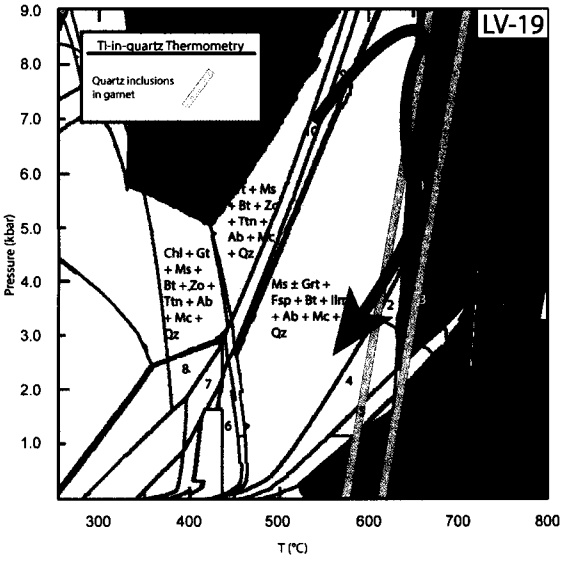

Appendix 3b: Pseudosections for garnet grade Deo Tibba gneiss LV-19 calculated using whole rock chemistry by Perple_X. Labels explained in App. 4a. Purple isopleths are Ti-in-biotite predictions by Perple_X (Ti concentrations in apfu for O=22), plotted along the same Ti range as microprobe data used in the thermometer. Single grain analyses of biotite from matrix and inclusions show decreasing temperature at the time of garnet growth, and an increasing temperature at the end of garnet growth.

Appendix 4a: Perple_X pseudosections for LV-2, LV-10 and LV-8. All phase diagrams are made in the hp11 database in the MnNCK-FMASHT system, saturated with SiO_2; H_20 cannot be a saturated component using melt(W). Ti-in-biotite thermometry is plotted as a thick green line(s) constraining the range of temperatures predicted by the thermometer, while purple lines are Ti concentrations (apfu) predicted by Perple_X. Thick blue lines with arrows show predicted P-T path for samples based on mineral field stability, Ti-in-biotite thermometry, and Ti-in-biotite predicted by Perple_X.

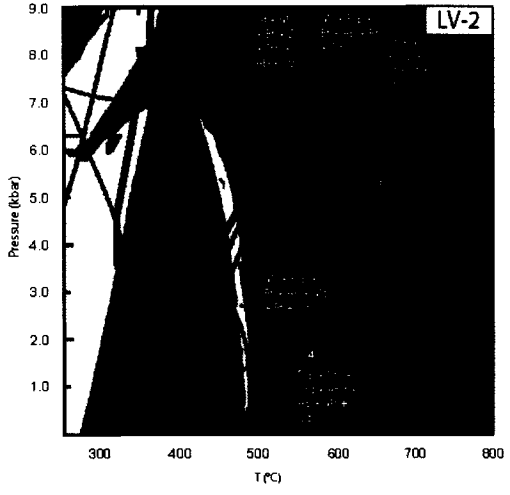

1. Chl + Gt + Ms + Bt + Zo + Ttn + Ab + Mc + Qz
2. Fsp + Chl + Ms + Ttn + Ab + Mc + Qz
3. Fsp + Chl + Ms + Ab + Mc + Rt + Qz
4. Ms + Fsp + Bt + Ilm + Crd + Ab + Mc + Rt + Qz
7. Ms + Fsp + Bt + Ttn + Ab + Mc + Qz
5. Grt + Ms + Fsp + Bt + Mc + Rt + Qz
6. Grt + Fsp + Bt + Sil + Mc + Rt + Qz

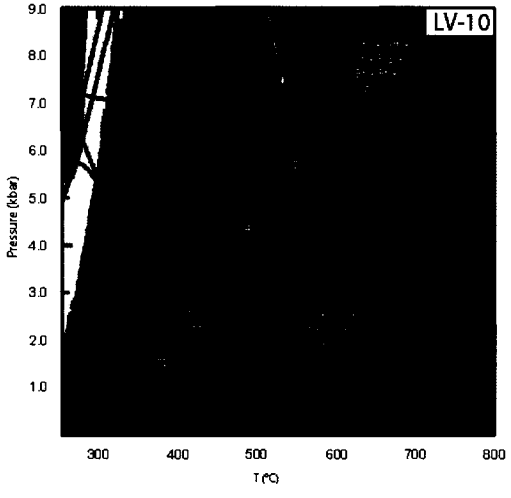

1. Chl + Ms + Fsp + Bt + Rt + Qz
2. Chl + Ms + Fsp + Bt + Rt + Qz
3. Chl + Ms + Fsp + Bt + Ab + Rt + Qz
4. Chl + Ms + Fsp + Ab + Rt + Qz
5. Chl + Ms + Fsp + Ab + Mc + Rt + Qz
6. Chl + Ms + Fsp + Ab + Mc + Rt + Qz
7. Chl + Fsp + Bt + Crd + Rt + Qz
8. Chl ± Grt + St + Fsp + Bt + Rt + Qz
9. Chl + Ms + Bt + Zo + Rt + Qz
10. Chl + Ms + Zo + Ttn + Ab + Qz
11. Fsp + Chl + Ms + Ttn + Ab + Qz
12. Chl + Ms + Ttn + Ab + Wrk + Qz

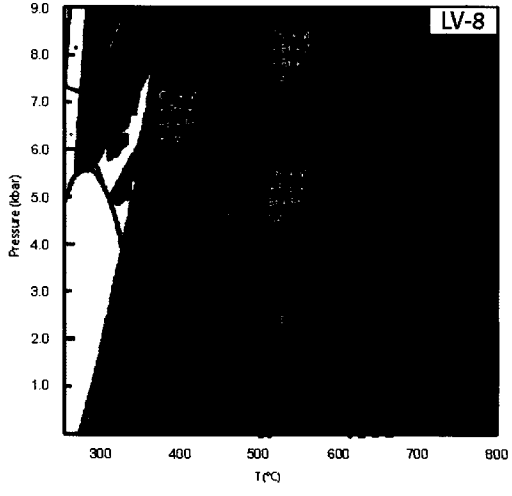

1. Chl ± Gt + Ms + Bt + Rt + Qz
2. Ms + St + Fsp + Bt + Rt + Qz
3. Ms + Fsp + Bt + Sil + Rt + Qz
4. Ms + Fsp + Bt + And + Rt + Qz
5. Chl + Ms + Fsp + Bt + Ilm + Rt + Qz
6. Chl + Ms + Fsp + Bt + Rt + Qz
7. Chl + Ms + Bt + Ttn + Ab + Rt + Qz
8. Chl + Ms + Mc + Hul + Rt + Qz
9. Chl + Ms + Ab + Mc + Hul + Rt + Qz
10. Chl + Ms + Fsp + Ab + Mc + Rt + Qz
11. Chl + Ms + Fsp + Ab + Mc + Rt + Qz

Appendix 4b: Perple_X pseudosections for LV-11, LV-15 and LV-9. All phase diagrams are made in the hp11 database in the MnNCKFMASHT system, saturated with SiO_2; H_20 cannot be a saturated component using melt(W). Ti-in-biotite thermometry is plotted as a thick green line(s) constraining the range of temperatures predicted by the thermometer, while purple lines are Ti concentrations (apfu) predicted by Perple_X. Thick blue lines with arrows show predicted P-T path for samples based on mineral field stability, Ti-in-biotite thermometry, and Ti-in-biotite predicted by Perple_X.

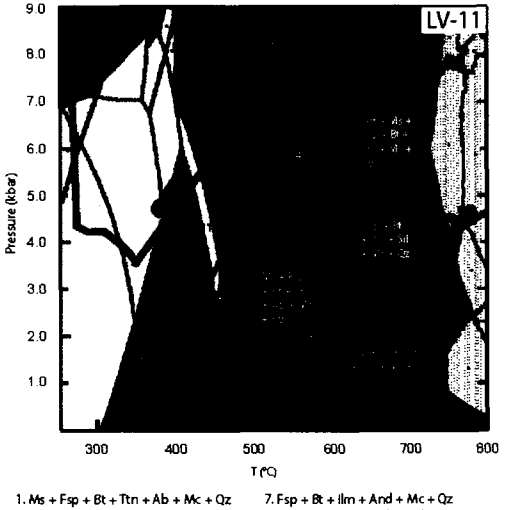

1. Ms + Fsp + Bt + Ttn + Ab + Mc + Qz
2. Ms + Fsp + Bt + Ab + Mc + Rt + Qz
3. Ms + Fsp + Bt + Mc + Rt + Qz
4. Ms + Fsp + Bt + Ab + Mc + Rt + Qz
5. Ms + Fsp + Bt + Ilm + Ab + Mc + Rt + Qz
6. Ms + Fsp + Bt + Ilm + Mc + Qz
7. Fsp + Bt + Ilm + And + Mc + Qz
8. Fsp + Bt + Ilm + Crd + And + Mc + Qz
9. Fsp + Bt + Ilm + And + Ab + Mc + Qz
10. Chl + Ms + Zo + Ttn + Ab + Mc + Qz
11. Chl + Ms + Bt + Zo + Ttn + Ab + Mc + Qz
12. Chl + Ms + Fsp + Bt + Ilm + Ab + Mc + Qz

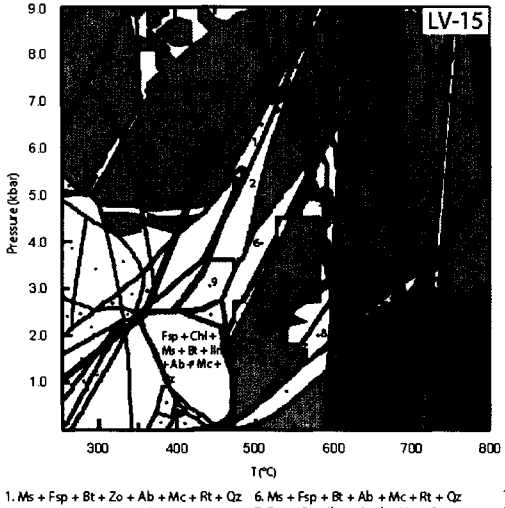

1. Ms + Fsp + Bt + Zo + Ab + Mc + Rt + Qz
2. Ms + Fsp + Bt + Ttn + Ab + Mc + Rt + Qz
3. Ms ± Grt + Fsp + Bt + Mc + Rt + Qz
4 Ms ± Grt + Fsp + Bt + Ilm + Ms + Rt + Qz
5. Ms + Fsp + Bt + Ilm + Ab + Mc + Qz
6. Ms + Fsp + Bt + Ab + Mc + Rt + Qz
7. Fsp + Bt + Ilm + And + Mc + Qz
8. Fsp + Bt + Ilm + And + Ab + Mc + Qz
9. Fsp + Ms + Bt + Ttn + Ab + Mc + Rt + Qz

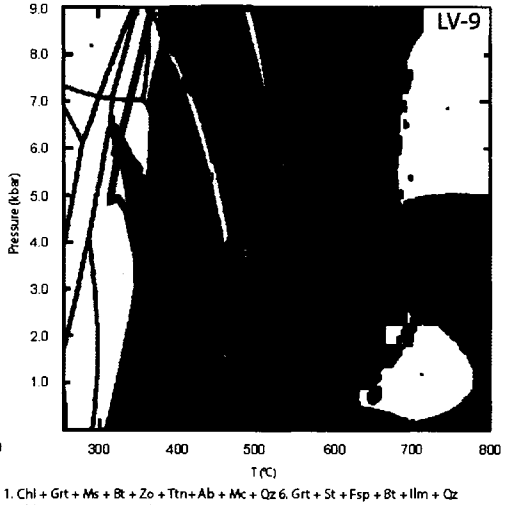

1. Chl + Grt + Ms + Bt + Zo + Ttn + Ab + Mc + Qz
2. Chl + Ms + Fsp + Bt + Ab + Rt + Qz
3. Chl + Ms + Fsp + Bt + Rt + Qz
4. Chl ± Grt + Ms + Fsp + Bt + Rt + Qz
5. Chl + Grt + St + Fsp + Bt + Ilm + Qz
6. Grt + St + Fsp + Bt + Ilm + Qz
7. Grt + Fsp + Bt + Ilm + Crd + Qz
8. Fsp + Grt + Bt + Ilm + Crd + Qz
9. Fsp + Chl + Gt + Bt + Ttn + Ab + Mc + Qz
10. Chl + Fsp + Bt + Ab + Mc + Rt + Qz